

University of Alberta

Simulation of Nano and Microfluidics Using a Lattice Boltzmann  
Method

by

Fuzhi Tian



A thesis submitted to the Faculty of Graduate Studies and Research in partial  
fulfillment of the requirements for the degree of **Master of Science**.

Department of Mechanical Engineering

Edmonton, Alberta

Fall 2004



Library and  
Archives Canada

Bibliothèque et  
Archives Canada

Published Heritage  
Branch

Direction du  
Patrimoine de l'édition

395 Wellington Street  
Ottawa ON K1A 0N4  
Canada

395, rue Wellington  
Ottawa ON K1A 0N4  
Canada

*Your file* *Votre référence*  
*ISBN: 0-612-95867-1*  
*Our file* *Notre référence*  
*ISBN: 0-612-95867-1*

The author has granted a non-exclusive license allowing the Library and Archives Canada to reproduce, loan, distribute or sell copies of this thesis in microform, paper or electronic formats.

L'auteur a accordé une licence non exclusive permettant à la Bibliothèque et Archives Canada de reproduire, prêter, distribuer ou vendre des copies de cette thèse sous la forme de microfiche/film, de reproduction sur papier ou sur format électronique.

The author retains ownership of the copyright in this thesis. Neither the thesis nor substantial extracts from it may be printed or otherwise reproduced without the author's permission.

L'auteur conserve la propriété du droit d'auteur qui protège cette thèse. Ni la thèse ni des extraits substantiels de celle-ci ne doivent être imprimés ou autrement reproduits sans son autorisation.

---

In compliance with the Canadian Privacy Act some supporting forms may have been removed from this thesis.

Conformément à la loi canadienne sur la protection de la vie privée, quelques formulaires secondaires ont été enlevés de cette thèse.

While these forms may be included in the document page count, their removal does not represent any loss of content from the thesis.

Bien que ces formulaires aient inclus dans la pagination, il n'y aura aucun contenu manquant.

# Canada

## ACKNOWLEDGEMENTS

First, I would like to thank my supervisor, Professor Daniel Y. Kwok, for his patient guidance, continual support and helpful suggestions in my research. Had he not given me the opportunity to join the Nanoscale Technology and Engineering Laboratory (NTEL), I doubt that I would have learned and enjoyed research as much as I used to.

I sincerely thank Professor Baoming Li for his initial involvement in directing me to this booming area: lattice Boltzmann simulation of electrokinetic transport phenomena. I am very grateful for his help and encouragement.

I wish to thank my wife, Mrs. Xuequn Wang, for her abundance of encouragement and support along my lengthy and wandering path through graduate school.

# TABLE OF CONTENTS

<b>1</b>	<b>Introduction</b>	<b>1</b>
1.1	The Study of Fluid Motions . . . . .	1
1.2	Numerical Methods in Fluid Study . . . . .	2
1.3	Electrokinetic Transport Phenomena . . . . .	5
1.4	Objectives . . . . .	6
1.5	Preview . . . . .	7
<b>2</b>	<b>Lattice Boltzmann Method</b>	<b>9</b>
2.1	Introduction . . . . .	9
2.2	Development of Lattice Boltzmann Model (LBM) . . . . .	10
2.2.1	From LGCA to LBM . . . . .	10
2.2.2	The BGK Approximation . . . . .	12
2.3	Derivation of a D2Q9 Lattice Boltzmann Model . . . . .	13
2.3.1	Discretization of Time . . . . .	13
2.3.2	Hydrodynamic Moments . . . . .	16
2.3.3	Lattice Boltzmann Equation on a D2Q9 Lattice . . . . .	17
2.4	External Force Term . . . . .	21
2.5	Boundary Conditions . . . . .	22
<b>3</b>	<b>Aspects of Nano and Microfluidics</b>	<b>26</b>

3.1	Introduction . . . . .	26
3.2	The Electrical Double Layer (EDL) . . . . .	26
3.3	Electrokinetic Transport Phenomena . . . . .	29
3.3.1	Pressure-Driven Flow . . . . .	30
3.3.2	Electroosmotic Flow . . . . .	31
3.4	Current Continuity . . . . .	32
3.5	EDL in Numerical Modelling . . . . .	33
<b>4</b>	<b>Simulation of Electroosmotic Flow with Uniform Zeta Potential</b>	<b>35</b>
4.1	Introduction . . . . .	35
4.2	Description of the Physical System . . . . .	37
4.3	Results and Discussion . . . . .	40
4.3.1	Effect of the Channel Height to the EDL Thickness Ratio: $\kappa H$ . . . . .	40
4.3.2	Effect of Electric Potential of the Solid Surface: $\psi_s$ . . . . .	43
4.3.3	Effect of Externally Applied Electric Field: $E_x$ . . . . .	44
4.4	Summary . . . . .	45
<b>5</b>	<b>Simulation of Electroosmotic Flow with Nonuniform Zeta Potential</b>	<b>46</b>
5.1	Introduction . . . . .	46
5.2	Description of the Physical System . . . . .	48
5.3	Results and Discussion . . . . .	51
5.3.1	Influence of the Nonuniform Surface Potential on the Velocity Profiles . . . . .	51

5.3.2	Influence of the Nonuniform Surface Potential on the Volumetric Flow Rate . . . . .	58
5.3.3	Trade-off between Mixing and Flow Efficiency of Microfluidics with Heterogeneous Surfaces . . . . .	61
5.4	Summary . . . . .	62
<b>6</b>	<b>Simulation of Electrokinetic Flows with Constraints of Current Continuity</b>	<b>63</b>
6.1	Introduction . . . . .	63
6.2	Description of the Physical System . . . . .	64
6.3	Results and Discussion . . . . .	67
6.3.1	Pressure-Driven Flow . . . . .	67
6.3.2	Electroosmotic Flow . . . . .	69
6.4	Summary . . . . .	74
<b>7</b>	<b>Conclusions and Future Work</b>	<b>76</b>
7.1	Summary of the Results . . . . .	76
7.2	Future Work . . . . .	77
	<b>Bibliography</b>	<b>79</b>

## LIST OF TABLES

3.1	EDL thickness of KCl solution with different ionic molar concentrations $C$ . . . . .	29
-----	---	----

## LIST OF FIGURES

2.1	Velocity vectors of a D2Q9 Lattice Boltzmann model; $\delta_x$ is the dimension of the lattice . . . . .	17
2.2	Periodic boundary. Particles leaving from the right to the left and vice versa : $f_\alpha \longrightarrow f'_\alpha$ ( $\alpha = 1 \sim 8$ ). . . . .	23
2.3	No-slip boundary condition: (a) On-grid bounce-back (b) Mid-grid bounce-back. . . . .	24
3.1	Schematic of an electric double layer near a plate wall and a particle. . . . .	26
3.2	Schematic of pressure-driven flow and $\oplus$ represents the net charges in the channel. . . . .	30
3.3	Schematic of electroosmosis and $\oplus$ represents the net charges in the channel. . . . .	32
4.1	Geometry of a rectangular microchannel with a length $L$ , width $W$ and height $H$ . . . . .	37
4.2	Electroosmotic velocity profiles for KCl solution with different ionic molar concentrations $C$ ( $C = 10^{-2}$ M, $10^{-3}$ M, $10^{-4}$ M, channel height $H = 50$ nm, $\psi_s = -25$ mV, $E_x = 250$ V/m). . . .	41



4.3	Electroosmotic velocity profiles for different channel heights $H$ ( $H = 50$ nm, 100 nm, 200 nm, 400 nm, 800 nm, $C = 10^{-4}$ M, $\psi_s = -25$ mV, $E_x = 1000$ V/m). . . . .	42
4.4	Electroosmotic velocity profiles for different surface potential in the same channel ( $H = 50$ nm, $C = 10^{-2}$ M, $E_x = 50$ V/m, $\kappa H = 16$ ). . . . .	43
4.5	Electroosmotic velocity profiles for different externally applied electric field in the same channel ( $H = 50$ nm, $C = 10^{-2}$ M, $\psi_s = -25$ mV, $\kappa H = 16$ ). . . . .	44
5.1	Schematic of the patterned surfaces with (a) a symmetric (b) asymmetric stepwise variation of surface potential. $\psi$ and $L$ are the surface potential and length of the heterogeneous patches, respectively. The subscripts $n$ and $p$ represent the negatively and positively charged surfaces, respectively. . . . .	48
5.2	Schematic of an electroosmotic flow near the double layer region for (a) a homogeneous surface and (b) a homogeneous surface with a heterogeneous patch. $1/\kappa$ is the double layer thickness. . . . .	50
5.3	Velocity profiles for a symmetrically arranged nonuniform surface potential when $\psi_n = -25$ mV and (a) $\psi_p = 0$ mV and $L_n/L_p = 1$ ; (b) $\psi_p = 20$ mV and $L_n/L_p = 1$ ; (c) $\psi_p = 25$ mV and $L_n/L_p = 1$ ; (d) $\psi_p = 0$ mV and $L_n/L_p = 4$ ; (e) $\psi_p = 75$ mV and $L_n/L_p = 4$ ; (f) $\psi_p = 100$ mV and $L_n/L_p = 4$ . . . . .	53

5.4 Velocity profiles for an asymmetrically arranged nonuniform surface potential when  $\psi_n = -25$  mV and (a)  $\psi_p = 0$  mV and  $L_n/L_p = 1$ ; (b)  $\psi_p = 20$  mV and  $L_n/L_p = 1$ ; (c)  $\psi_p = 25$  mV and  $L_n/L_p = 1$ ; (d)  $\psi_p = 0$  mV and  $L_n/L_p = 4$ ; (e)  $\psi_p = 75$  mV and  $L_n/L_p = 4$ ; (f)  $\psi_p = 100$  mV and  $L_n/L_p = 4$ . . . . . 56

5.5 Normalized volumetric flow rate versus surface potential of the positively charged region  $\psi_p$  when  $\psi_n = -25$  mV. Curve A represents the case of  $L_n/L_p = 4$  and  $\psi_p = 0, 25, 50, 75,$  and  $100$  mV; Curve B represents the case of  $L_n/L_p = 1$  and  $\psi_p = 0, 5, 10, 15, 20,$  and  $25$  mV. . . . . 59

5.6 Normalized volumetric flow rate versus length ratio of the positively charged region  $L_p/(L_p + L_n)$  for  $\psi_p = |\psi_n| = 25$  mV. . . . 60

5.7 Normalized volumetric flow rate versus average surface potential  $\psi_{avg}$  when  $\psi_n = -25$  mV and  $\square$ :  $L_n/L_p = 1$  and  $\psi_p = 0, 5, 10, 15, 20,$  and  $25$  mV;  $\blacklozenge$ :  $\psi_p = 25$  mV and  $L_p/(L_p + L_n) = 0, 0.2, 0.4,$  and  $0.5$ ;  $\circ$ :  $L_n/L_p = 4$  and  $\psi_p = 0, 25, 50, 75,$  and  $100$  mV. 61

6.1 Geometry of a 2D heterogeneous microchannel, consisting of two different sections.  $\psi_1$  and  $\psi_2$  are the two stepwise variation of surface potentials for the heterogeneous channel. . . . . 65

6.2 Streaming potential along a 1 cm rectangular microchannel ( $H = 500$  nm) with a uniform surface potential for  $\psi = -25$  to  $-100$  mV, in a 25 mV increment. The pressure gradient is  $dP/dx = 10$  MPa/m. . . . . 68

6.3	Streaming potential along a 1 cm rectangular microchannel ( $H = 500$ nm) with a nonuniform surface potential for $\psi_2 = -25$ to $-100$ mV, in a 25 mV increment. The pressure gradient is $dP/dx = 10$ MPa/m. . . . .	69
6.4	Distribution of potential along a 1 cm rectangular microchannel ( $H = 500$ nm) with a stepwise variation of surface potential ( $\psi_1 = 0$ mV and $\psi_2 = -5$ mV.) when the constraint of current continuity is considered in electroosmotic flow . . . . .	71
6.5	An electrical circuit analogy to electroosmotic flow in heterogeneous microchannel in Figure 6.1. . . . .	72
6.6	Normalized potential at the junction of the two heterogeneous sections in Figure 6.1 versus the surface potential of the right section $\psi_2$ with current continuity when $\psi_1 = 0$ mV and $\phi_1 = 100$ V. . . . .	73
6.7	Normalized volumetric flow rate in electroosmotic flow versus the surface potential of the right section $\psi_2$ with and without the constraint of current continuity . . . . .	74

## NOMENCLATURE

$A_c$  ..... Cross-section Area of Channels

$c_s$  ..... Speed of Sound

$C$  ..... Ionic Molar Concentration

$D$  ..... Dimension of the Space

$e$  ..... Elementary Charge ( $1.602 \times 10^{-19}$  C)

$\mathbf{E}$  ..... Electric Field Strength

$f$  ..... Particle Distribution Function

$f^{eq}$  ..... Particle Equilibrium Distribution Function

$\mathbf{F}$  ..... External Body Force

$H$  ..... Height of Channels

$I_{cb}$  ..... Bulk Conduction Current

$I_{cs}$  ..... Surface Conduction Current

$I_s$  ..... Streaming Current

$I_t$  ..... Total Current

$K_b$  ..... Boltzmann Constant ( $1.381 \times 10^{-23} \text{JK}^{-1}$ )  
 $L$  ..... Length of Channels  
 $n_i$  ..... Ionic Number Concentration of  $i$ th Species  
 $n_\infty$  ..... Ionic Number Concentration at the Neutral State where  $\psi = 0$   
 $N_i(x, t)$  ..... Boolean Particle Distribution  
 $P$  ..... Pressure  
 $P_w$  ..... Wetted Perimeter of Channels  
 $R$  ..... Gas Constant ( $8.314 \text{JK}^{-1} \text{mol}^{-1}$ )  
 $t$  ..... Time  
 $T$  ..... Temperature  
 $\mathbf{V}$  ..... Velocity Vector  
 $u$  ..... Velocity in  $x$ -direction  
 $U(x)$  ..... Potential Energy of the Conservative Force field  
 $W$  ..... Width of Channels  
 $z_i$  ..... Valence of Type- $i$  Ions  
 $\delta$  ..... Knudsen Number  
 $\delta_t$  ..... Time Step  
 $\varepsilon$  ..... Dimensionless Dielectric Permittivity of Electrolyte Solution

$\epsilon_0$ .....	Dielectric Permittivity of Vacuum ( $8.8542 \times 10^{-12} \text{C}^2 \text{N}^{-1} \text{m}^{-2}$ )
$\phi$ .....	Streaming Potential or Imposed Electric Potential
$\frac{1}{\kappa}$ .....	Debye Length
$\lambda$ .....	Relaxation Time
$\lambda_b$ .....	Bulk Conductivity
$\lambda_d$ .....	Length of Mean Free path
$\lambda_s$ .....	Surface Conductivity
$\mu$ .....	Viscosity
$\nu$ .....	Kinematic Viscosity ( $\nu = \frac{\mu}{\rho}$ )
$\rho$ .....	Density of the Aqueous Solution
$\rho_e$ .....	Net Charge Density
$\tau$ .....	Dimensionless Relaxation Time
$\Omega(f)$ .....	Collision Function
$\xi$ .....	Particle Velocity
$\psi$ .....	Electrical Potential
$\psi_s$ .....	Electrical Surface Potential
$\Psi$ .....	Total Electrical Potential, $\Psi = \psi + \phi$
$\zeta$ .....	Zeta Potential

# CHAPTER 1

## INTRODUCTION

### 1.1 The Study of Fluid Motions

From the aspects of dimension, fluid flows can take a variety of forms ranging from nano, micro to macroflows. Both liquid and gaseous flows have been the subject of fluid motions. Nevertheless, it is advantageous to develop a numerical model capable of effectively simulating the motion of different flows.

In the community of traditional fluid dynamics, fluid motion is described by the continuity equation

$$\frac{\partial \rho}{\partial t} + \nabla \cdot (\rho \mathbf{V}) = 0 \quad (1.1)$$

and the Navier-Stokes equations

$$\frac{\partial(\rho \mathbf{V})}{\partial t} + \rho \mathbf{V} \cdot \nabla \mathbf{V} = -\nabla P + \mu \nabla^2 \mathbf{V} + \mathbf{F} \quad (1.2)$$

where  $\mathbf{V}$  is the velocity vector,  $\rho$  is the density of the solution,  $P$  is the pressure,  $\mu$  is the viscosity of the solution and  $\mathbf{F}$  represents another external force except the pressure  $P$ . The Navier-Stokes equation is a second-order partial differential equation which does not have a known analytic solution except for a small number of special cases. Fortunately, the advent of computer technology makes

it possible to solve the Navier-Stokes equation numerically for fluid flows.

## 1.2 Numerical Methods in Fluid Study

Traditional Computational Fluid Dynamics (CFD) has developed many numerical techniques to solve the continuity equations (1.1) and Navier-Stokes equation (1.2) or similar equations according to different situations. Some alternative methods are also available.

### Numerical Solution of the Navier-Stokes Equations

The most popular method in CFD is the numerical solution of equations (1.1) and (1.2). Given the continuity and Navier-Stokes equations and a set of suitable boundary conditions, it is possible to solve the problems on a grid via the standard numerical methods and techniques such as finite volume, finite difference and finite element. This works well for simple flows while more complex problems usually require a more complex approach. There are many standard texts on numerical methods in fluids including J. H. Ferziger et.al [1], P. Roch [2] and J. Connor et.al.[3], etc..

### Molecular Dynamics (MD)

Molecular Dynamics is a direct method to simulate a fluid by modelling the individual molecules which make up the fluid. The system should behave as a fluid [4], provided the inter-molecular interactions, such as van der Waals interaction, are modelled correctly. Different situations can be modelled by changing the average energy of the molecules and their separation.

The main disadvantages with such an approach are that large computer resources are required and many simulations take hours to evolve a fraction



of a second [5]. The system must also be updated in small time-steps, new position and velocity of all particles being calculated from a knowledge of their previous position and velocity, taking into account any external forces which act on them. Any particles which collided during the previous time-step have to be identified and their new trajectories calculated. This is strictly time consuming when considering even a very small volume of fluid. Even when a gas is being considered where there are fewer molecules and a larger time-step, the number of molecules which can be considered is severely limited.

### **Direct Simulation Monte Carlo (DSMC)**

Direct Simulation Monte Carlo (DSMC), which was first proposed by Bird [6] for the simulation of rarefied gas flows, is a direct particle simulation method based on kinetic theory. The fundamental idea is to track a large number of statistically representative particles. The particle motion and interactions are then used to modify their positions, velocities, or chemical reactions. Conservation of mass, momentum, and energy is enforced to machine accuracy. The primary approximation of DSMC is to uncouple the molecular motions and the intermolecular collisions over small time intervals. Particle motions are modeled deterministically, while the collisions are treated statistically. Symmetries in physical space can be used to reduce the number of grid dimensions and the storage requirements for molecular spatial information.

However, modeling collision is always a three-dimensional calculation. The limitations of DSMC are the same as those of classical kinetic theory: the assumption of molecular chaos and the restriction to dilute gases. More details are available in Oran *et. al.*'s review paper [7].

## Lattice Boltzmann Model (LBM)

Over the past ten years, a new method for the computer simulation of fluids has been developed: the lattice gas model [8, 9]. Instead of considering a large number of individual molecules in the molecular dynamics approach, a much smaller number of fluid particles are considered. A fluid particle is a large group of molecules which although much larger than a molecule is still considerably smaller than the smallest length scale of the simulation. This reduces the amount of data which needs to be stored since large simulations can be performed using less than one million particles. In a lattice gas model, the particles are restricted to move on the links of a regular underlying grid and the motion evolves in discrete time-steps. The conservation laws are incorporated into update rules which are applied at each discrete time.

A lattice gas model in which the state of the fluid needs to be known only at the lattice sites and only at discrete times can run much faster in a computer than a MD or DSMC simulation. The lattice gas model has another big advantage since all collisions occur at the same time. This is a particular advantage if the simulation is being run on parallel computers. These two time saving advantages of the lattice gas model allow simulations in a significantly larger scale to be performed.

The Lattice Boltzmann model (LBM) has evolved from the lattice gas model. There are a number of difficulties, for instance, the lack of Galilean invariance and large collision matrices, with the lattice gas approach to fluid modelling. Various modifications have been made to overcome these difficulties and the outcome is the LBM. As the name suggests, this technique involves simulating

the Boltzmann equation

$$\frac{\partial f}{\partial t} + \boldsymbol{\xi} \cdot \nabla f + \mathbf{G} \cdot \nabla_{\boldsymbol{\xi}} f = \Omega(f) \quad (1.3)$$

where  $\Omega(f)$  is a collision function,  $\mathbf{G}$  is the body force per unit mass,  $\boldsymbol{\xi}$  is the particle velocity and  $f$  is the distribution function. The distribution function is a statistical parameter from which the macroscopic properties of the fluid can be found. The simulation of the Boltzmann equation is performed on a regular lattice and the form of the collision function  $\Omega(f)$  is taken to be the BGK collision operator which was first considered to represent collisions in the non-discrete Boltzmann equation [10]. The computation reflects the evolution from the lattice gas model. The model is updated in the same manner as the lattice gas model except that, instead of considering individual particles to be travelling along the links, it is the distribution function which is evolved. The LBM has the advantages associated with the lattice gas model and all the lattice gas difficulties have been overcome. Thus, LBM is an ideal tool in fluid simulation, especially in complex fluid.

### 1.3 Electrokinetic Transport Phenomena

The first discovery of electrokinetic phenomena occurred about two centuries ago. In 1808, Reuss [11] discovered electroosmotic effects and Quinke [12] discovered the streaming potential phenomenon in 1859. Electrokinetic theory is widely applied to many fields such as chemistry, chemical engineering, aerospace science, biology, medicine, environment, civil and mechanical engineering. Electrokinetic phenomena are essential issues in colloid and interface/surface science, playing important roles in industry: mining, ceramics, paints, pharmaceuticals,

paper making, waste water treatment and petroleum.

In general, when a solid surface is immersed in an aqueous solution, a double layer of electrical charges (also known as the electrical double layer, or EDL) near to the interface will be formed between the liquid and solid wall where counter-ions and co-ions in an aqueous solution are preferentially distributed so that the net charge density is non-zero [13–15]. It is the net charge or the EDL that induces the electrokinetics including four principal phenomena: streaming potential, electroosmosis, electrophoresis and sedimentation potential. For pressure-driven flow, the effect of EDL during an externally applied pressure gradient is to retard liquid flow, also known as an electroviscous effect, and induce a streaming potential at equilibrium [16, 17]. When an electric field is applied between two ends of the channel, the excess counter-ions in the EDL will be driven by the electric body force and pull the liquid due to viscous force, resulting in an electroosmotic flow. Motion of charged particles in a stationary electrolyte under an externally applied electric field is called electrophoresis which can be used as species separation. A sedimentation potential is created, when charged particles are moved under gravitational or centrifugal fields.

#### **1.4 Objectives**

Numerical studies of electrokinetic transport phenomena in nano and microfluidic system have followed the traditional route, common to most numerical problems, of solving the modified Navier-Stokes equations subject to a set of boundary and initial conditions. However, this traditional method has many difficulties in these complex phenomena occurring in the region of electrical double layer. Since the complexity of nano and microfluidic systems is essentially due to the microscopic interparticle interactions, the LBM simulation provides

an excellent alternative to model such complex fluid dynamics problems [18–21].

Therefore, the main objectives of this thesis are:

1. To show the lattice Boltzmann model (LBM) by incorporating an external force is an effective computational tool to simulate pressure-driven and electroosmotic flows in nano and microchannels;
2. To investigate effect of nonuniform surface potential on mixing and flow rate in nano and microchannels;
3. To study influence of nonuniform surface potential on potential distribution along flow direction and flow rate in nano and microchannels with requirements of flow rate and current continuity;
4. To compare the results of the simulations with the theoretical predictions and existing experimental results.

## 1.5 Preview

In Chapter 2, the development of LBM will be reviewed and the details of LBM scheme in the thesis will be given.

In Chapter 3, the basic idea of EDL theory and the corresponding governing equations will be presented. Furthermore, the induced electrokinetic transport phenomena by EDL will be discussed.

In Chapter 4, electroosmotic flows in straight rectangular channels are simulated by the LBM in the presence of an externally applied electric field. Effects of channel height, electrolyte concentration, surface potential, electric double layer thickness and applied electric field on the velocity profile will be studied and compared with the corresponding analytical solutions.

In Chapter 5, the LBM is used to simulate flow field in a rectangular microchannel with nonuniform (step change) surface potentials. The simulation results indicate that local circulations can occur near a heterogeneous region with nonuniform surface potentials, in agreement with those by other authors. Largest circulations, which imply a highest mixing efficiency due to convection and short-range diffusion, were found when the average surface potential is zero, regardless of whether the distribution of the heterogeneous patches is symmetric or asymmetric. More importantly, it is illustrated that there is a trade-off between the mixing and flow efficiency in EOF microfluidics. One should not simply focus on mixing and neglect liquid transport, as performed in the literature. Excellent mixing could lead to a poor transport of electroosmotic flow in microchannels.

In Chapter 6, the LBM coupled with the constraint of current continuity is utilized to simulate the microfluidic flow field in a rectangular microchannel with a step variation of surface potentials. This current continuity has often been neglected in electroosmotic flow regarding nonuniform (heterogeneous) microchannels. Results show that step variation of ion distribution caused by step variation surface potential will influence significantly the electrical potential distribution along the channel and volumetric flow rate. The volumetric flow rate could have been overestimated by as much as 70% without consideration of the current continuity constraint.

Finally, in Chapter 7, conclusions are summarized and future work is outlined.

## CHAPTER 2

### LATTICE BOLTZMANN METHOD

#### 2.1 Introduction

In recent years, the Lattice Boltzmann Method (LBM) has been developed in a state that it can be an alternative and promising numerical scheme for fluid flow simulation and modeling physics in fluids. This method evolved from the lattice gas model known as Lattice Gas Cellular Automata (LGCA) [8]. Both are methods for the simulation of fluid flows which are distinctive from molecular dynamics (MD) or Direct Simulation Monte Carlo (DSMC) on the one hand and methods based on the discretization of partial differential equations (finite difference, finite volumes, finite elements, and spectral method) on the other. The principle of the LBM is to construct a dynamical system on a simple lattice involving a number of quantities that can be interpreted as a single-particle distribution function of fictitious particles on the link of a lattice. These quantities then evolve at each time step through a two-step procedure. The first step is to advance the fluid particles to the next lattice site along their direction of motion. The second step is to simulate particle collisions by relaxing the distribution toward an equilibrium distribution using a linear relaxation parameter. The macroscopic density, velocity and energy are calculated as the

moment of the single-particle distribution functions. The obvious advantages of the LBM are the parallelism of the approach [22–25], the simplicity of the programming, and the capability of easily incorporating microscopic interactions [26–29]. In this chapter, the development of the LBM will be reviewed and a Lattice Boltzmann equation with an external force term and a corresponding equilibrium distribution function for microfluidics will be derived [30].

## 2.2 Development of Lattice Boltzmann Model (LBM)

### 2.2.1 From LGCA to LBM

The LBM originated from LGCA, which is a discrete lattice kinetics utilizing a discrete lattice and discrete time. LGCA was proposed by J. Conway [31]. The first LGCA model called HPP model was given in 1973 by Hardy, Pomeau and de Pazzis [32, 33]. The name was derived from the names of the three authors. Although the HPP model conserves mass and momentum, it does not yield the desired Navier-Stokes equation in the macroscopic limit. In 1986, Frisch, Hasslacher and Pomeau showed that a LGCA model over a lattice with a larger symmetry yields the incompressible Navier-Stokes equation in the macroscopic limit [34]. This model with hexagonal symmetry is named FHP according to the names of the three authors. The discovery of the symmetry constraint was the start for a rapid development of lattice-gas methods. The theoretical foundations were worked out by Wolfram [35] and by Frisch et al. [36].

The FHP model on hexagonal lattice is governed by

$$N_i(x + \xi_i \Delta t, t + \Delta t) = N_i(x, t) + \Omega(N_i(x, t)), \quad i = 1 \dots 6 \quad (2.1)$$

where  $N_i(x, t)$  is the boolean particle distribution representing the presence/absence



of a particle with velocity  $\xi_i(x, t)$ ,  $\Omega(N_i(x, t))$  is the collision operator reflecting the collision rules by which particles interact on the nodes. These collision rules must satisfy mass and momentum conservation. It was shown that microscopic collision rules applied in FHP lead to the following macroscopic equation [37]

$$\frac{\partial \mathbf{V}}{\partial t} = -(g(\rho)\mathbf{V} \cdot \nabla)\mathbf{V} - \frac{1}{\rho}\nabla P + \nu\nabla^2\mathbf{V} \quad (2.2)$$

where  $\mathbf{V}$  is the velocity vector,  $\rho$  is the density (average number of particles on the node),  $\nu$  is the kinematic viscosity. Eq. (2.2) resembles the Navier-Stokes equation for incompressible fluids, except for the fact that there is a density function  $g(\rho)$  in front of the convection term ( $g(\rho) = \frac{\rho-3}{\rho-6}$  for FHP model). This artifact is known as non-Galilean invariance of LGCA. To cope with this unphysical effect, the rest particles were introduced in FHP II model, allowing one to set the non-Galilean term close to unity. The central ideas in the papers contemporary with the FHP papers include the cellular automaton model [35] and the 3D model using four-dimensional face-centered-hyper-cubic (FCHC) lattice [38].

In these early LGCA models, a boolean particle distribution was used. Therefore, at this point, one major artifact of all the LGCA models was the statistical noise due to boolean value dynamics. This led to the averaging over large number of lattice points and time steps to produce smooth flow field. The main feature of the LBM is replacing the boolean particle distribution values by particle distribution function and thus reducing the statistical noise and neglecting individual particle motion and particle-particle correlation in the kinetic equations [39]. Historically the following stages in the development of the LBM can be distinguished:

1. Lattice Boltzmann equations have been used already at the cradle of lattice-gas cellular automata by Frisch et al. to calculate the viscosity of LGCA in 1987 [36].
2. Lattice Boltzmann model as an independent numerical method for hydrodynamic simulations was introduced by McNamara and Zanetti in 1988 [39]. The motivation for moving from LGCA to LBM was to reduce statistical noise. The Boolean fields were replaced by continuous distributions over the FHP and FCHC lattices; Fermi-Dirac distributions were used as equilibrium functions.
3. Linearized collision operator was introduced by Higuera and Jimenez in 1989 [40].
4. Boltzmann instead of Fermi-Dirac distributions is used to avoid the non-Galilean invariance of LGCA.
5. The collision operator has been replaced by the BGK (also called single time relaxation) approximation by Koelman in 1991 [41] , Qian et al. in 1992 [42] and others.

The lattice BGK models mark a new level of abstraction: collisions are not anymore defined explicitly.

### **2.2.2 The BGK Approximation**

One of the major problems when dealing with the Boltzmann equation (1.3) is the complicated nature of the collision function  $\Omega(f)$ . It is therefore not surprising that alternative, simpler expressions have been proposed. The idea behind this replacement is that a large amount of the detail of the two-body

interaction, which is contained in the Boltzmann collision operator, is unlikely to influence significantly the values of the macroscopic quantities [43]. Any replacement collision function must satisfy the conservation of mass, momentum and energy.

Based on the assumptions that the particle distribution can be expanded about its local equilibrium state [36, 44] and that the local particle distribution relaxes to equilibrium state at a single-time-relaxation rate [10, 42, 45, 46], the linearized form of collision function  $\Omega(f)$  can be obtained

$$\Omega_i(f) = -\frac{1}{\lambda}(f_i - f_i^{eq}) \quad (2.3)$$

where  $f_i^{eq}$  is the equilibrium distribution function depending on local macroscopic variables, i.e.  $\rho$  and  $\mathbf{V}$ , and the relaxation time  $\lambda$ . This model is frequently called the BGK model after Bhatnagar, Gross and Krook who first introduced it in 1954 [10].

## 2.3 Derivation of a D2Q9 Lattice Boltzmann Model

### 2.3.1 Discretization of Time

He *et al.* [19, 20] showed that the Lattice Boltzmann equation can be directly derived from the continuous Boltzmann equation discretized in some special manner in both time and phase space. The continuous Boltzmann equation with a single-relaxation-time as a collision model discussed in section 2.2.2 is given by

$$\frac{\partial f}{\partial t} + \xi \cdot \nabla f + \mathbf{G} \cdot \nabla_{\xi} f = -\frac{f - f^{eq}}{\lambda} \quad (2.4)$$

For a steady fluid immersed in a conservative force field, the equilibrium distribution function is defined by adding a Boltzmann factor to the Maxwell-Boltzmann distribution [47]

$$f^{eq} = \frac{\rho_0}{(2\pi c_s^2)^{D/2}} \exp\left(-\frac{U(x)}{K_b T}\right) \exp\left(-\frac{(\xi - \mathbf{V})^2}{2c_s^2}\right) \quad (2.5)$$

where  $U(x)$  is a potential energy of conservative force field,  $\rho_0$  is the density of the fluid when  $U(x)$  is equal to 0,  $K_b$  is the Boltzmann constant,  $T$  is the temperature,  $c_s$  and  $D$  are the speed of sound in a fluid and dimensionality of space, respectively. The macroscopic density  $\rho$ , velocity  $\mathbf{V}$ , and energy  $\epsilon$  are calculated as the moment of the distribution function  $f$

$$\rho = \int f d\xi \quad \rho \mathbf{V} = \int \xi f d\xi \quad \rho \epsilon = \frac{1}{2} \int (\xi - \mathbf{V})^2 f d\xi \quad (2.6)$$

Martys et al. [48] have pointed out that  $\mathbf{G} \cdot \nabla_\xi f$  is identical to  $\mathbf{G} \cdot \nabla_\xi f^{eq}$  up to the second order because the first two Hermite coefficients of the distribution function are always the same as those in the local Maxwellian distribution. Thus, by assuming  $\nabla_\xi f \approx \nabla_\xi f^{eq} = -\frac{\xi - \mathbf{V}}{c_s^2} f^{eq}$ ,

$$\frac{\partial f}{\partial t} + \xi \cdot \nabla f + \frac{1}{\lambda} f = \left(\frac{1}{\lambda} + \frac{\mathbf{G} \cdot (\xi - \mathbf{V})}{c_s^2}\right) f^{eq} \quad (2.7)$$

can be obtained consequently. Eq. (2.7) can be formally rewritten in the form of an ordinary differential equation

$$\frac{df}{dt} + \frac{1}{\lambda} f = \frac{1}{\lambda'} f^{eq} \quad (2.8)$$

where

$$\frac{d}{dt} = \frac{\partial}{\partial t} + \xi \cdot \nabla \quad (2.9)$$

is the time derivative along the characteristic line  $\xi$ , and

$$\frac{1}{\lambda'} = \frac{1}{\lambda} + \frac{\mathbf{G} \cdot (\xi - \mathbf{V})}{c_s^2} \quad (2.10)$$

is the reciprocal of equivalent relaxation time due to the action of external force.

The above inhomogeneous ordinary differential equation can be integrated over a small time step of  $\delta_t$

$$\begin{aligned} f(x + \xi\delta_t, \xi, t + \delta_t) = & \exp\left(-\frac{\delta_t}{\lambda}\right) \int_0^{\delta_t} \frac{1}{\lambda'} \exp\left(\frac{t'}{\lambda}\right) f^{eq}(x + \xi t', \xi, t + t') dt' + \\ & \exp\left(-\frac{\delta_t}{\lambda}\right) f(x, \xi, t) \end{aligned} \quad (2.11)$$

Assuming that  $\delta_t$  is small enough and  $f^{eq}$  is smooth enough locally, the following first-order approximation can be made

$$\begin{aligned} f^{eq}(x + \xi t', \xi, t + t') = & f^{eq}(x, \xi, t) + \frac{t'}{\delta_t} \{f^{eq}(x + \xi\delta_t, \xi, t + \delta_t) - \\ & f^{eq}(x, \xi, t)\} + O(\delta_t^2), \quad t' \in [0, \delta_t] \end{aligned} \quad (2.12)$$

Therefore, Eq. (2.11) becomes

$$\begin{aligned} f(x + \xi\delta_t, \xi, t + \delta_t) = & \frac{1}{\lambda'} \exp\left(-\frac{\delta_t}{\lambda}\right) \left\{ \lambda \left( \exp\left(\frac{\delta_t}{\lambda}\right) - 1 \right) f^{eq}(x, \xi, t) + \right. \\ & \frac{\lambda^2}{\delta_t} \left( \left( \frac{\delta_t}{\lambda} - 1 \right) \exp\left(\frac{\delta_t}{\lambda}\right) + 1 \right) (f^{eq}(x + \xi\delta_t, \xi, t + \delta_t) - \\ & \left. f^{eq}(x, \xi, t)) \right\} + \exp\left(-\frac{\delta_t}{\lambda}\right) f(x, \xi, t) \end{aligned} \quad (2.13)$$

Substituting the Taylor expansion of the term  $\exp\left(\pm \frac{\delta_t}{\lambda}\right)$  into Eq. (2.13) and neglecting the term of order  $O(\delta_t^2)$  or smaller, then Eq. (2.13) is simplified as

$$f(x + \xi\delta_t, \xi, t + \delta_t) - f(x, \xi, t) = -\frac{1}{\tau} \left( f(x, \xi, t) - \frac{\lambda}{\lambda'} f^{eq}(x, \xi, t) \right) \quad (2.14)$$

where  $\tau = \frac{\lambda}{\delta_t}$  is a dimensionless relaxation time. Eq. (2.14) is the evolution equation of the distribution function  $f(x, \xi, t)$  with discrete time.

### 2.3.2 Hydrodynamic Moments

Although  $f^{eq}$  is expressed as an explicit function of time  $t$ , the time dependence of  $f^{eq}$  is solely through hydrodynamics variable  $\rho$ ,  $\mathbf{V}$ , and  $T$ . Namely,  $f^{eq}(x, \xi, t) = f^{eq}(x, \xi, \rho, \mathbf{V}, T)$ . Therefore,  $\rho$ ,  $\mathbf{V}$ , and  $T$  must be computed before constructing the equilibrium distribution function  $f^{eq}$  so that the calculation of  $\rho$ ,  $\mathbf{V}$ , and  $T$  becomes one of the most crucial steps in discretizing the Boltzmann equation.

To numerically evaluate the hydrodynamic moments of Eq. (2.6), appropriate discretization in momentum space  $\xi$  must be accomplished, i.e.

$$\int \psi(\xi) f^{eq}(x, \xi, t) d\xi = \sum_{\alpha} W_{\alpha} \psi(\xi_{\alpha}) f^{eq}(x, \xi_{\alpha}, t) \quad (2.15)$$

where  $\psi(\xi)$  is a polynomial of  $\xi$ ,  $W_{\alpha}$  is a weighted coefficient of the quadrature, and  $\xi_{\alpha}$  is the discrete velocity set or the abscissas of the quadrature. Accordingly, the hydrodynamic moments of Eq. (2.6) can be computed by

$$\rho = \sum_{\alpha} f_{\alpha} \quad \rho \mathbf{V} = \sum_{\alpha} \xi_{\alpha} f_{\alpha} \quad \rho \epsilon = \frac{1}{2} \sum_{\alpha} (\xi_{\alpha} - \mathbf{V})^2 f_{\alpha} \quad (2.16)$$

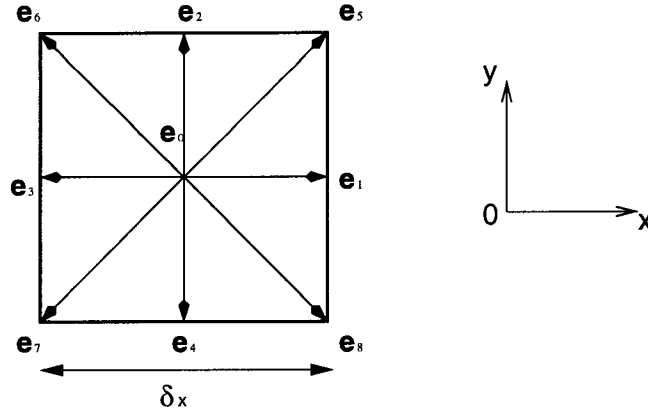


Figure 2.1: Velocity vectors of a D2Q9 Lattice Boltzmann model;  $\delta_x$  is the dimension of the lattice

where  $f_\alpha \equiv f_\alpha(x, t) \equiv W_\alpha f(x, \xi_\alpha, t)$ .

### 2.3.3 Lattice Boltzmann Equation on a D2Q9 Lattice

The Lattice Boltzmann equation has three ingredients: (1) an evolution equation, in the similar form of Eq. (2.14) with discretized time and phase space in which configuration space is of a lattice structure and the momentum space is reduced to a small set of discrete momenta; (2) conservation constraints in the form of the hydrodynamic moments; (3) a proper equilibrium distribution function which leads to the Navier-Stokes equations [8]. In what follows, the low Mach number expansion is applied to the Maxwell-Boltzmann distribution function with a Boltzmann factor. In the Lattice Boltzmann equation, the equilibrium distribution function  $f^{eq}(x, \xi, t)$  is obtained by a truncated small

velocity expansion

$$\begin{aligned}
f^{eq}(x, \xi, t) &= \frac{\rho_0}{(2\pi c_s^2)^{D/2}} \exp\left(-\frac{U(x)}{K_b T}\right) \exp\left(-\frac{\xi^2}{2c_s^2}\right) \exp\left(\frac{\xi \cdot \mathbf{V}}{c_s^2} - \frac{\mathbf{V}^2}{2c_s^2}\right) \\
&= \frac{\rho_0}{(2\pi c_s^2)^{D/2}} \exp\left(-\frac{U(x)}{K_b T}\right) \exp\left(-\frac{\xi^2}{2c_s^2}\right) \\
&\quad \times \left(1 + \frac{\xi \cdot \mathbf{V}}{c_s^2} + \frac{(\xi \cdot \mathbf{V})^2}{2c_s^4} - \frac{\mathbf{V}^2}{2c_s^2}\right) + O(\mathbf{V}^3)
\end{aligned} \tag{2.17}$$

The equilibrium distribution function with truncated small velocity expansion is used as follows

$$\begin{aligned}
f^{eq}(x, \xi, t) &\approx \frac{\rho_0}{(2\pi c_s^2)^{D/2}} \exp\left(-\frac{U(x)}{K_b T}\right) \exp\left(-\frac{\xi^2}{2c_s^2}\right) \\
&\quad \times \left(1 + \frac{\xi \cdot \mathbf{V}}{c_s^2} + \frac{(\xi \cdot \mathbf{V})^2}{2c_s^4} - \frac{\mathbf{V}^2}{2c_s^2}\right)
\end{aligned} \tag{2.18}$$

Calculating the hydrodynamic moments of  $f^{eq}$  is equivalent to evaluating the following integral in general

$$\begin{aligned}
I = \int \psi(\xi) f^{eq}(x, \xi, t) d\xi &= \frac{\rho_0}{(2\pi c_s^2)^{D/2}} \exp\left(-\frac{U(x)}{K_b T}\right) \int \psi(\xi) \exp\left(-\frac{\xi^2}{2c_s^2}\right) \\
&\quad \times \left(1 + \frac{\xi \cdot \mathbf{V}}{c_s^2} + \frac{(\xi \cdot \mathbf{V})^2}{2c_s^4} - \frac{\mathbf{V}^2}{2c_s^2}\right) d\xi
\end{aligned} \tag{2.19}$$

If a two-dimensional Lattice Boltzmann model with nine discrete velocities on a square grid of dimensions  $\delta_x$  (D2Q9 LBM) shown in Figure 2.1 is considered, the microscopic velocity  $\xi$  in the continuous Boltzmann equation can be



expressed as the discrete velocities  $e_\alpha$  as follows

$$e_\alpha = \begin{cases} (0, 0) & \alpha = 0 \\ \left( \cos \left[ \frac{\pi(\alpha - 1)}{2} \right], \sin \left[ \frac{\pi(\alpha - 1)}{2} \right] \right) c & \alpha = 1, 2, 3, 4 \\ \left( \cos \left[ \frac{\pi(\alpha - 5)}{2} + \frac{\pi}{4} \right], \sin \left[ \frac{\pi(\alpha - 5)}{2} + \frac{\pi}{4} \right] \right) \sqrt{2}c & \alpha = 5, 6, 7, 8 \end{cases} \quad (2.20)$$

where  $\alpha$  is the notation of the 9-bit discrete velocities shown in Figure 2.1,  $c = \frac{\delta_x}{\delta_t} = \sqrt{3}c_s$ , and  $\delta_x$  and  $\delta_t$  are the lattice constant and time step size, respectively. To order the 9-bit LBM model on a square lattice space, the Cartesian coordinate system is used and, accordingly,  $\psi(\xi)$  can be set to

$$\psi_{m,n} = \xi_x^m \xi_y^n \quad (2.21)$$

where  $\xi_x$  and  $\xi_y$  are the  $x$  and  $y$  component of  $\xi$ . The integral of the moments in Eq. (2.19) can be rewritten as

$$I = \frac{\rho_0}{\pi} \exp \left( - \frac{U(x)}{K_b T} \right) (\sqrt{2}c_s)^{m+n} \times \left\{ \left( 1 - \frac{V^2}{2c_s^2} \right) I_m I_n + \frac{2(V_x I_{m+1} I_n + V_y I_m I_{n+1})}{\sqrt{2}c_s} + \frac{V_x^2 I_{m+2} I_n + 2V_x V_y I_{m+1} I_{n+1} + V_y^2 I_m I_{n+2}}{c_s^2} \right\} \quad (2.22)$$

where

$$I_m = \int_{+\infty}^{-\infty} \varsigma^m \exp(-\varsigma^2) d\varsigma, \quad \varsigma = \frac{\xi}{\sqrt{2}c_s} \quad (2.23)$$

$I_m$  is the  $m$ th order moment of the weight function  $\exp(-\varsigma^2)$  on the real axis. The third-order Hermite formula is the optimal choice to evaluate  $I_m$  for the

purpose of deriving the 9-bit LBM model

$$I_m = \sum_{j=1}^3 \omega_j \zeta_j^m \quad (2.24)$$

The three abscissas of the quadrature are

$$\varsigma_1 = -\sqrt{\frac{3}{2}}, \quad \varsigma_2 = 0, \quad \varsigma_3 = \sqrt{\frac{3}{2}} \quad (2.25)$$

and the corresponding weighted coefficients are

$$\omega_1 = \frac{\sqrt{\pi}}{6}, \quad \omega_2 = \frac{2\sqrt{\pi}}{3}, \quad \omega_3 = \frac{\sqrt{\pi}}{6} \quad (2.26)$$

Then, the integral of the moment in Eq. (2.22) becomes

$$I = \frac{\rho_0}{\pi} \exp\left(-\frac{U(x)}{K_b T}\right) \sum_{i,j=1}^3 \omega_i \omega_j \psi(\xi_{i,j}) \times \left(1 + \frac{\xi \cdot \mathbf{V}}{c_s^2} + \frac{(\xi \cdot \mathbf{V})^2}{2c_s^4} - \frac{\mathbf{V}^2}{2c_s^2}\right) \quad (2.27)$$

where  $\xi_{i,j} = (\xi_i, \xi_j)$ . The equilibrium distribution can be identified from the above equation

$$I = \frac{\omega_i \omega_j}{\pi} \rho_0 \exp\left(-\frac{U(x)}{K_b T}\right) \left(1 + \frac{\xi \cdot \mathbf{V}}{c_s^2} + \frac{(\xi \cdot \mathbf{V})^2}{2c_s^4} - \frac{\mathbf{V}^2}{2c_s^2}\right) \quad (2.28)$$

By employing the notation of the 9-bit discrete velocities and the weight coefficients, the equilibrium function of the 9-bit LBM model can be obtained

$$f_\alpha^{eq} = \omega_\alpha \rho_0 \exp\left(-\frac{U(x)}{K_b T}\right) \left[1 + \frac{(e_\alpha \cdot \mathbf{V})}{c_s^2} + \frac{(e_\alpha \cdot \mathbf{V})^2}{2c_s^4} - \frac{\mathbf{V}^2}{2c_s^2}\right] \quad (2.29)$$

where

$$\omega_\alpha = \frac{\omega_i \omega_j}{\pi} = \begin{cases} \frac{4}{9} & i = j = 2 & \alpha = 0 \\ \frac{1}{9} & i = 1, j = 2, \dots & \alpha = 1, 2, 3, 4 \\ \frac{1}{36} & i = j = 1, \dots & \alpha = 5, 6, 7, 8 \end{cases} \quad (2.30)$$

Thus, the evolution equation Eq. (2.14) can be rewritten as

$$\begin{aligned} f_\alpha(x + e_\alpha \delta_t, e_\alpha, t + \delta_t) - f_\alpha(x, e_\alpha, t) \\ = -\frac{1}{\tau} \left\{ f_\alpha(x, e_\alpha, t) - \left( 1 + \tau \delta_t \frac{(e_\alpha - \mathbf{V}) \cdot \mathbf{G}}{c_s^2} \right) f_\alpha^{eq} \right\} \end{aligned} \quad (2.31)$$

The hydrodynamic moments on the square lattice can be computed by

$$\rho = \sum_{\alpha=0}^8 f_\alpha \quad \rho \mathbf{V} = \sum_{\alpha=0}^8 e_\alpha f_\alpha \quad \rho \epsilon = \frac{1}{2} \sum_{\alpha=0}^8 (e_\alpha - \mathbf{V})^2 f_\alpha \quad (2.32)$$

and according to the Lattice Boltzmann model, the kinematic viscosity can be expressed as

$$\nu = \frac{2\tau - 1}{6} \frac{\delta_x^2}{\delta_t} \quad (2.33)$$

and the Navier-Stokes equation can be derived from Eq. (2.29) and (2.31) through the Chapman-Enskog method [8, 49].

## 2.4 External Force Term

In the Lattice Boltzmann equation, the external force term  $\mathbf{G} = \frac{\mathbf{F}}{\rho}$  where  $\mathbf{F}$  can be expressed as

$$\mathbf{F} = \mathbf{F}_{ext} + q_\alpha (\mathbf{E}_{int} + \boldsymbol{\xi} \times \mathbf{B}_{int}) + \mathbf{F}_V \quad (2.34)$$

where  $\mathbf{F}_{ext}$  represents the external forces, including pressure and Lorentz force associated with any externally applied electric and magnetic fields;  $\mathbf{E}_{int}$  and  $\mathbf{B}_{int}$  are internally smoothed electric and magnetic fields due to the motion of all charged particles inside the fluid, respectively;  $\mathbf{F}_V$  is a single equivalent force due to intermolecular attraction. In the case of an electrokinetic flow, if gravity and any induced magnetic field are negligible, the body force  $\mathbf{F}$  depends only on the externally applied pressure and induced electric field for pressure-driven flow. For electroosmotic flow,  $\mathbf{F}$  depends on the externally applied electric field and ion distribution in the channels. For example, the external force in electroosmotic flow can be calculated by

$$\mathbf{F} = \rho_e \mathbf{E}_{ext} \quad (2.35)$$

where  $\rho_e$  is the net charge density at any point in the liquid and  $\mathbf{E}_{ext}$  the externally applied electric field strength.

## 2.5 Boundary Conditions

The boundary conditions (BC), playing a crucial role in LBM method, are distinguished into two basic classes : Elementary and Complex [25]. Elementary implies that the physical boundary is aligned with the grid coordinates and the distinctive mark is that the mesh cells are not cut through. A staircase approximation is used for complex surfaces. Complex boundaries, on the contrary, can take virtually any shape, including mesh-cutting surface. Consequently, they can describe complex shapes more accurately, making it more difficult to implement. In this thesis, only the elementary boundary condition is utilized because of the simple shape of the rectangular channel. In the following part, periodic

and no-slip boundary conditions for elementary boundaries will be reviewed. Other boundary conditions which are not used in this thesis, such as free-slip, sliding walls, and open inlet/outlets, can be found in the book by Sauro Succi [25].

### Periodic Boundary Condition

The periodic boundary condition is one of the simplest boundary conditions. It is typically intended to isolate bulk phenomena from the actual boundaries of the real physical system and consequently it is adequate for physical phenomena where surface effects play a negligible role. In nano and microfluidics, if the inlet and outlet effect are not to be considered, the periodic boundary condition is a good choice. As shown in Figure 2.2, particles leave from the right to the left

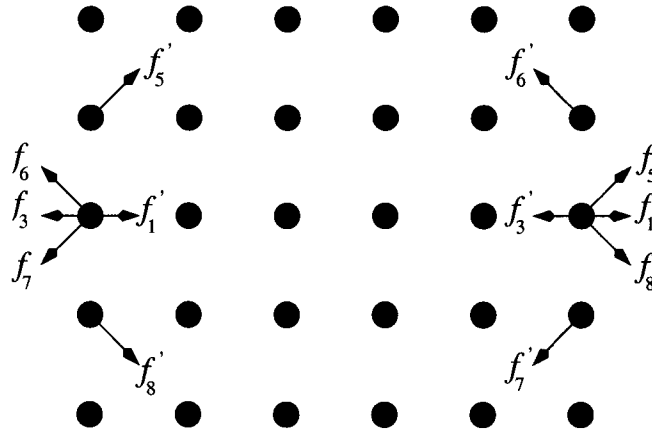


Figure 2.2: Periodic boundary. Particles leaving from the right to the left and vice versa :  $f_\alpha \longrightarrow f'_\alpha$  ( $\alpha = 1 \sim 8$ ).

and vice versa according to the advection rules, namely,  $f_\alpha \longrightarrow f'_\alpha$  ( $\alpha = 1 \sim 8$ ).

## No-slip Boundary Conditions

Another simplest boundary condition is the so-called “no-slip” situation, namely, zero fluid velocity at a given solid surface. In the LBM method, there are two types of implementations: on-grid [25, 50–53] and mid-grid [25, 54]. The on-grid condition means that the physical boundary lies exactly on the grid node, whereas the mid-grid case refers to the situation where the boundary lies in between two grid lines or on the links.

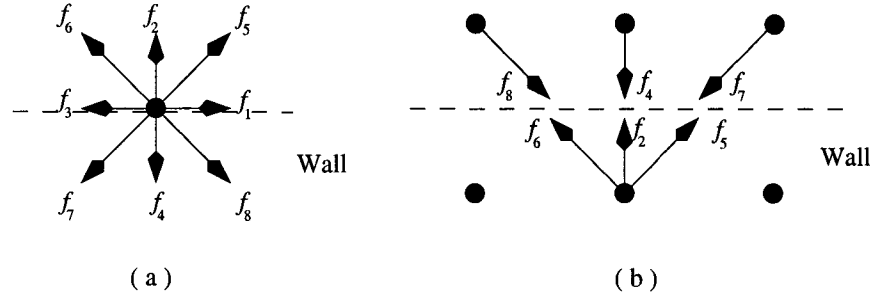


Figure 2.3: No-slip boundary condition: (a) On-grid bounce-back (b) Mid-grid bounce-back.

As shown in Figure 2.3 (a), the on-grid bounce-back just reverses all populations sitting on a boundary node after advection to obtain the unknown distributions  $f_2$ ,  $f_5$  and  $f_6$

$$f_2(x, y) = f_4(x, y) \quad f_5(x, y) = f_7(x, y) \quad f_6(x, y) = f_8(x, y) \quad (2.36)$$

The mid-grid bounce-back scheme shown in Figure 2.3 (b) reads:

$$f_2(x, y) = f_4(x+1, y+1) \quad f_5(x, y) = f_7(x+1, y+1) \quad f_6(x, y) = f_8(x+1, y+1) \quad (2.37)$$

Obviously, the other wall is handled in the same way.

In the LBM algorithm in this thesis, the on-grid bounce-back boundary condition at the wall is applied for a no-slip boundary condition; the periodic boundary condition is used at the outlet and inlet for the flexibility that the results in a short section can be extended to a long channel. The drawback of the periodic boundary condition is the inability to simulate inlet and outlet effects.

## CHAPTER 3

### ASPECTS OF NANO AND MICROFLUIDICS

#### 3.1 Introduction

In nano and microfluidic systems, the key aspects include the electric double layer (EDL) and the induced electrokinetic transport phenomena such as streaming potential, electroosmosis, electrophoresis, etc. In this chapter, the basic idea of EDL theory and electrokinetic transport phenomena will be presented.

#### 3.2 The Electrical Double Layer (EDL)

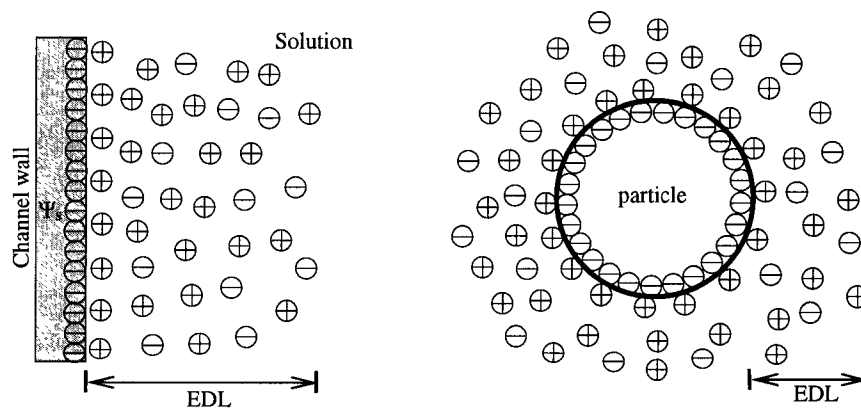


Figure 3.1: Schematic of an electric double layer near a plate wall and a particle.



In general, when a solid surface is immersed in an aqueous solution, a double layer of electrical charges (also known as the electrical double layer, or EDL) near to the interface will be formed between the liquid and solid wall where counter-ions and co-ions in an aqueous solution are preferentially distributed so that the net charge density is non-zero [13–15]. It is the net charge or the EDL that induces the electrokinetics including four principal phenomena: streaming potential, electroosmosis, electrophoresis and sedimentation potential. Two schematic diagram for electric double layer near a plate and particle are shown in Figure 3.1. Given the surface is negatively charged, the density of the counter-ions (cation) is higher than that of the co-ion (anion) in the EDL region near to the wall or the particle surface. The thickness of the EDL is normally regarded as the distance from the solid surface to a position where the net charge decreases to zero (neutral solution).

The concept of double layer was introduced by Helmholtz in 1879 [55] . In the early 1900s, the diffusive double layer was developed independently by Gouy [56] and Chapman [57] . Usually, the EDL is divided into two layers: an inner/compact layer of immobile counter-ions and a diffusion layer with transitions from the extreme excess of counter-ions at the boundary of the immobile layer to a balance of counter-ions and co-ions in the neutral bulk solution. The potential at the interface between the inner layer and diffusion layer is called zeta potential (surface potential) whose characteristic is the key point of the electrokinetic phenomena. Depending on different materials being in contact with an aqueous solution, the interfacial charges originate from various mechanism: ionization of surface group, charged crystal surface, specific ion adsorption, etc. [13, 15, 58].

Mathematically, Poisson-Boltzmann equation is the most popular model to

describe the ionic and potential distribution in EDL [13, 15, 58]. According to electrostatic theory, the potential is governed by the Poisson equation

$$\nabla^2\psi = -\frac{\rho_e}{\varepsilon\varepsilon_0} \quad (3.1)$$

where  $\psi$  is the electric potential due to the EDL,  $\rho_e$  is the net charge density,  $\varepsilon$  is the dimensionless dielectric permittivity of electrolyte solution and  $\varepsilon_0$  is the dielectric permittivity of vacuum. Assuming that the Boltzmann distribution applies, the equilibrium Boltzmann distribution equation can be used to describe the ionic concentration as follows

$$n_i = n_\infty \exp\left(-\frac{z_i e}{K_b T} \psi\right) \quad (3.2)$$

where  $n_i$  is the ionic number concentration of the  $i$ th species,  $z_i$  is the valence of type- $i$  ions,  $n_\infty$  is the ionic number concentration at the neutral state where  $\psi = 0$ , and  $e$  is the elementary charge. The charge density can be expressed in terms of Boltzmann distribution for a symmetric electrolyte, i.e.  $z_+ = z_- = z$ , and is given by

$$\rho_e = -2n_\infty z e \sinh\left(\frac{ze}{K_b T} \psi\right) \quad (3.3)$$

Substituting the above expression into Eq. (3.1), the nonlinear Poisson-Boltzmann equation is obtained

$$\nabla^2\psi = \frac{2n_\infty z e}{\varepsilon\varepsilon_0} \sinh\left(\frac{ze}{K_b T} \psi\right) \quad (3.4)$$

If  $ze\psi/K_b T$  is small (i.e.,  $|\psi| \leq 25$  mV),  $\sinh(ze)\psi/K_b T \approx ze\psi/K_b T$ ; whereby

Table 3.1: EDL thickness of KCl solution with different ionic molar concentrations  $C$

Ionic molar concentration: $C$ (M)	EDL thickness: $\frac{1}{\kappa}$ (nm)
$10^{-2}$	3.04
$10^{-3}$	9.62
$10^{-4}$	30.40
$10^{-5}$	96.20

the Debye-Hückel approximation is invoked, Eq. (3.3) can be rewritten as

$$\rho_e = -\frac{2n_\infty z^2 e^2}{K_b T} \psi \quad (3.5)$$

and Eq. (3.4) can be linearized as

$$\nabla^2 \psi = \frac{2n_\infty z^2 e^2}{\varepsilon \varepsilon_0 K_b T} \psi = \kappa^2 \psi \quad (3.6)$$

where

$$\kappa^2 = \frac{2n_\infty z^2 e^2}{\varepsilon \varepsilon_0 K_b T} \quad (3.7)$$

and  $\frac{1}{\kappa}$ , called Debye length for a  $z : z$  electrolyte, represents the thickness of EDL. In Table 3.1, the EDL thickness of KCl solution with different ionic molar concentrations  $C$  are given. In fact, Debye-Hückel approximation gives a good agreement with experiments when surface potential is up to 100 mV [13].

### 3.3 Electrokinetic Transport Phenomena

Electrokinetics is a phenomenon associated with the movement of the bulk electrolyte solution or a liquid carrying a free charge relative to a stationary charged surface under the influence of an externally applied force such as gravity, pressure and electric field [58]. In practice, channels used in nano or microfluidic

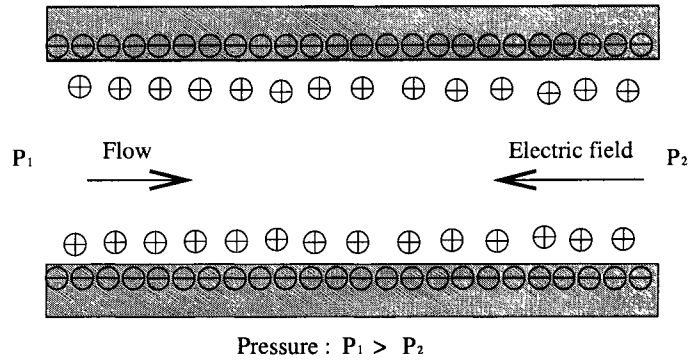


Figure 3.2: Schematic of pressure-driven flow and  $\oplus$  represents the net charges in the channel.

devices are fabricated by means of modern micromachining technology. The cross section of these channels resembles a rectangular shape [59]. Thus, research on electrokinetic transport phenomena in a straight rectangular channel is important. Electrokinetic transport phenomena in channels are usually divided into three groups: pressure-driven flow, electroosmotic flow and electrophoresis. In this thesis, the first two phenomena are considered by the LBM because pressure-driven and electroosmotic flow are the two main methods for pumping solution in most microfluidics applications. In this section, the basic concept and the relative phenomena of pressure-driven and electroosmotic flows are presented briefly.

### 3.3.1 Pressure-Driven Flow

When a fluid is forced through a channel under an applied pressure gradient, the counter-ions in the mobile part of the electric double layer (EDL) are carried toward the downstream end (Figure 3.2), so that an electric current called the streaming or convection current is induced in the pressure-driven flow direction. Corresponding to this streaming current, an electrokinetic potential

named streaming potential is built up along the channel. This flow-induced streaming potential acts to drive the counter-ions in the mobile part of the EDL to move in the direction opposite to the streaming current, i.e., opposite to the pressure-driven flow direction, generating an electrical current called conduction current. The motion of the ions will cause the liquid to move, resulting in a liquid flow against the pressure-driven flow. Therefore, compared to the flow rate predicted by the traditional fluid mechanics theory without EDL effect, the flow rate here is reduced; the liquid would appear to have a higher viscosity. This is usually referred to as an electroviscous effect [16, 17].

An important parameter for the strength of the streaming potential or the electroviscous effect is the thickness of the EDL. As shown in Eq. (3.7), the EDL thickness  $\frac{1}{\kappa}$  increases when ion concentration decreases, which implies that the largest effects of the streaming potential can be expected for de-ionized water (which contains a small but finite ion concentration). Consequently, by adding salt to increase the ion concentration, the EDL-thickness can be made very thin and thus minimizing the opposing force due to the streaming potential. Therefore, the effect of EDL is neglected in macroscopic channels where the EDL thickness is relatively small. However, when the EDL thickness is comparable with the characteristic size of the flow channel, this effect can be significant.

### 3.3.2 Electroosmotic Flow

When an electric field is applied between two ends of the channel, the excessive counter-ions (net charges) in the EDL will be driven by the electric body force and these ions pull the liquid due to viscous drag force, resulting in an electroosmotic flow (Figure 3.3). The characteristics of the electroosmotic flow in a microchannel depend on the nature of the surface potential, i.e., whether

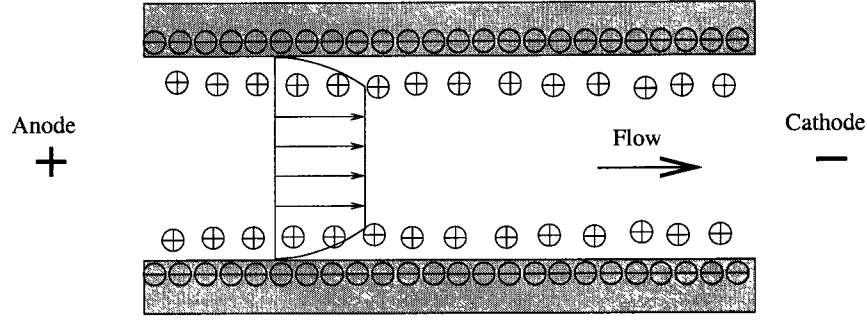


Figure 3.3: Schematic of electroosmosis and  $\oplus$  represents the net charges in the channel.

it is uniform or nonuniform.

### 3.4 Current Continuity

From the electrokinetic theory, the total current in the steady state consists of three components: bulk conduction current  $I_{cb}$ , surface conduction current  $I_{cs}$ , and convection current  $I_s$  [58, 60, 61]. The total current  $I_t$  can be calculated by

$$I_t = I_s + I_{cb} + I_{cs} \quad (3.8)$$

The convection current  $I_s$  for a slit rectangular channel shown in Figure 4.1 is defined by

$$I_s = \int_0^H u_x(x, y) \rho_e(x, y) W dy \quad (3.9)$$

In the above equation,  $u_x I_s = \int_0^H u_x(x, y) \rho_e(x, y) W dy$  in  $x$  direction, which changes in the  $y$  direction for microflows with uniform surface potential; while  $u_x(x, y)$  changes in both the  $x$  and  $y$  directions with nonuniform surface potential. Thus, with the knowledge of net ion distribution and velocity profile, the convection current can be evaluated. The conduction current  $I_c$  includes two

parts:  $I_{cb}$  and  $I_{cs}$ , and can be calculated by

$$I_c = I_{cb} + I_{cs} = A_c \lambda_b \frac{\phi}{L} + P_w \lambda_s \frac{\phi}{L} = (\lambda_b + \lambda_s \frac{P_w}{A_c}) A_c \frac{\phi}{L} \quad (3.10)$$

where  $A_c$  and  $P_w$ , respectively, are the cross-section area and wetted perimeter of the channel,  $\lambda_b$  is the bulk conductivity,  $\phi$  is the streaming potential in pressure-driven flow or the imposed electric potential in electroosmotic flow by setting the potential at the outlet to be 0 V, and  $\lambda_s$  is the surface conductivity. For a rectangular cross section channel with  $\frac{H}{W} \ll 1$  shown in Figure 4.1,  $\frac{P_w}{A_c} \approx \frac{2}{H}$ ; thus Eq. (3.10) can be simplified to

$$I_c = WH(\lambda_b + \frac{2\lambda_s}{H}) \frac{\phi}{L} \quad (3.11)$$

The surface conductance effects can be neglected when the channel is large (e.g.  $H > 200 \mu\text{m}$ ).

### 3.5 EDL in Numerical Modelling

Generally, numerical modelling of electrokinetic flow in nano- or microchannels is complicated due to the Debye-Hückel EDL thickness, of the order of a few nanometers shown in Table 3.1, when the geometrical parameters in submicron or micrometer range. It is intractable to take into account the ratio between two geometry parameters because discretization of the geometry would require an enormous computer memory. One method to solve this problem is by artificially inflating the order of EDL thickness to that of the channel dimension and therefore a qualitative and relative description can be given instead of a real quantitative one [62, 63]. The second approach is by applying a slip boundary

condition [64] . By this method, the EDL length scale is eliminated completely and description of the EDL is no longer needed. However, it is well-known that the electrical body force responsible for electroosmotic flow depends on the local net-charge density. Therefore, in this simulation, the Poisson-Boltzmann equation is solved to describe the potential and ion distribution in the EDL and the real dimension of EDL is used in the LBM.



## CHAPTER 4

# SIMULATION OF ELECTROSMOTIC FLOW WITH UNIFORM ZETA POTENTIAL

### 4.1 Introduction

Computer simulations of fluid dynamics problems involving nano and microscale surface interactions are of both fundamental and practical importance in the development of Micro-Electro-Mechanical Systems (MEMS) and Lab-on-Chip devices [65–67]. Typically, the above mentioned microfluidic systems consist of a thin glass plate with a network of microchannels etched into the surface. In these channels, the electrolyte solution is in contact with the glass plate surface, which is generally the charged plane. Thus, counter-ions accumulate near the plane and co-ions deplete from this region, thereby creating a EDL in the solution near the wall. This EDL plays a key role in microfluidic transport phenomena, such as electroosmosis. The EDL thickness, which is from several nanometers to a few hundreds of nanometers depending on the ionic concentration of the electrolyte solution (see table 3.1), is small in comparison with the height of microchannels, but is in the same order of the height of nanochannels. The interfacial electrokinetic and wettability are strongly related to the interfacial

properties and geometry so that adequate description of fluid in microchannels is not an easy task. Traditional computational fluid dynamics (CFD) method which relies on the use of the Navier-Stokes equations [62, 68–70] has many difficulties in simulating such phenomena due to the presence of an electric double layer.

Currently, several alternative approaches are available to simulate microflows. First, a popular method is the Direct Simulation Monte Carlo (DSMC) algorithm. Many articles [6, 7, 71] present an extended review of the DSMC method for low-pressure rarefied gas flow applications; while Oran *et al.* [7] addressed its use on the microfluidic application. Although DSMC is popular for analysis of high-speed rarefied gas flow, it is not effective for simulation of gas or liquid microflows. It suffers from slow convergence and large statistical noise, and requires extensive number of simulated molecules. An alternative to the DSMC method is a Molecular Dynamics (MD) method which can be used to simulate liquid flow [72]. Many researchers employ this method to simulate the electroosmosis in nano-diameter channels [73, 74]. However, since MD requires modeling of every molecule, it is computational expensive and is usually applied to very small channel systems. For a smaller channel system, e.g., a 2-nm-wide channel, the MD simulation can be done fairly quickly; while for a larger system, e.g., a 6-nm-wide channel, the efficiency of this method is low.

Since the complexity of nano and microfluidic systems is essentially due to the microscopic interparticle interactions, the LBM simulation provides an excellent alternative to model such complex fluid dynamics problems [18–21]. The LBM, which can recover the Navier-Stokes equations from the discrete lattice Boltzmann equation with sufficient lattice symmetry, has a relatively simple algorithm and is an alternative to the solution of the Navier-Stokes equations

[42, 75]. Recently, a discrete Lattice Boltzmann equation was introduced for liquid microflows with electrokinetic transport phenomena by Li *et al.* [47]. In addition, the LBM has been used to simulate electro-viscous effects on pressure-driven liquid flow in microchannels and excellent agreement with experimental results was found [30, 76–78] .

In this chapter, electroosmotic flows in straight rectangular nano and microchannels are simulated via the LBM in the presence of an externally applied electric field. Effects of the channel height, electrolyte concentration, surface potential, electric double layer thickness and applied electric field on the velocity profile will be studied and compared with the corresponding analytical solutions.

## 4.2 Description of the Physical System

### Electrical field

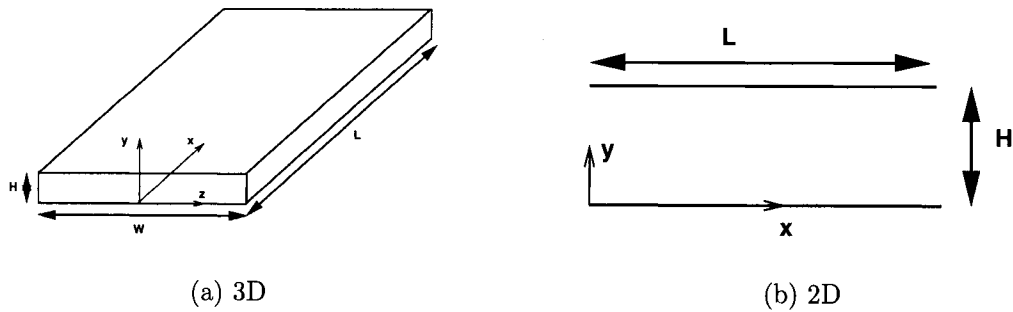


Figure 4.1: Geometry of a rectangular microchannel with a length  $L$ , width  $W$  and height  $H$ .

The electroosmotic flow to be considered in this chapter is fully developed, i.e., no end effects are present. The channel geometry is depicted in Figure 4.1. This rectangular microchannel has a length  $L$ , width  $W$  and height  $H$ .

The height-to-width ratio in the channel is much less than 1, allowing us to assume a two-dimensional flow and neglect any influence of the side walls on the polarization of the electrolyte and the flow field.

In the electroosmotic flow, the electric field is governed by the Poisson equation

$$\nabla^2 \Psi = -\frac{\rho_e}{\varepsilon \varepsilon_0} \quad (4.1)$$

where  $\Psi$  is the total electric potential. In general, ion concentration is affected by both the distribution of the externally applied potential in electroosmotic flow or streaming potential in pressure-driven flow,  $\phi$ , and the distribution of the potential,  $\psi$ , associated with the electrical double layer with surface potential,  $\psi_s$ . If one assumes that the ion distribution near the wall is unaffected by  $\phi$  and the principle of superposition for the potential is available, the total electric potential,  $\Psi$ , is given by the summation of the surface potential and the externally applied potential or the streaming potential, i.e.,  $\Psi = \psi + \phi$ . Therefore, Eq. (4.1) can be rewritten as a Laplace equation

$$\nabla^2 \phi = 0 \quad (4.2)$$

which is used to control the externally applied electric field or the streaming potential along the channel, and the Poisson equation (3.1) in Chapter 3 for the potential distribution in the EDL region. In a straight channel with uniform surface potential, the governing equations for the ion distribution essentially reduce to a one-dimensional problem. Therefore, Eqs. (3.6) with the Debye-Hückel approximation may be simplified as

$$\frac{d^2 \psi}{dy^2} = \frac{2n_\infty z^2 e^2}{\varepsilon \varepsilon_0 k_b T} \psi = \kappa^2 \psi \quad (4.3)$$

The boundary conditions for solving the Poisson-Boltzmann equation (4.3), are given by

$$\psi = \psi_s \text{ at } y = 0, H \quad \text{and} \quad \frac{d\psi}{dy} = 0 \text{ at } y = \frac{H}{2} \quad (4.4)$$

Eq. (4.3) is a linear one-dimensional ordinary differential equation that can be solved analytically, subjected to the boundary conditions given in Eq. (4.4). The net charge density at any point in the channel can be obtained using Eq. (3.5) after the electrical potential distribution  $\psi$  has been found.

### Flow Field by Navier-Stokes Equations

The general Navier-Stokes equation for incompressible steady flow is given by

$$\rho \mathbf{V} \cdot \nabla \mathbf{V} = -\nabla \mathbf{P} + \mu \nabla^2 \mathbf{V} + \mathbf{F} \quad (4.5)$$

For a steady-state, one-dimensional and fully developed flow, the velocity components are described by  $u = u(y)$ ,  $v = 0$  and  $w = 0$ . Additionally, if the flow is driven by an externally applied electric field rather than a pressure, the first term on the right hand side of Eq. (4.5) drops out. Thus, the general Navier-Stokes equation (4.5) can be simplified to

$$\mu \frac{d^2 u}{dy^2} = -F_x \quad (4.6)$$

where  $F_x$  is the body force due to the externally applied electric field  $E_x$ . The relationship between  $F_x$  and the electric field strength  $E_x$  is given by

$$F_x = \rho_e E_x \quad (4.7)$$

Substituting Eqs. (3.5) and (4.7) into Eq. (4.6) yields

$$\mu \frac{d^2 u}{dy^2} = \frac{2n_\infty z^2 e^2}{k_b T} \psi E_x \quad (4.8)$$

The boundary conditions for this one-dimensional problem are

$$u = 0 \text{ at } y = 0, H \quad \text{and} \quad \frac{du}{dy} = 0 \text{ at } y = \frac{H}{2} \quad (4.9)$$

The electric strength  $E_x$  can be obtained by solving Laplace equation (4.2). Finally, Eq. (4.6) can be solved analytically and the solution subjected to the boundary conditions above is given by

$$u(y) = -\frac{\varepsilon \varepsilon_0 \psi_s E_x}{\mu} \left( 1 - \frac{e^{\kappa y} + e^{\kappa H - \kappa y}}{1 + e^{\kappa H}} \right) \quad (4.10)$$

### 4.3 Results and Discussion

In this section, simulation results are presented for the effect of the channel height to the EDL thickness ratio  $\kappa H$ , the electric potential of the solid surface  $\psi_s$ , and the externally applied electric field  $\phi$  on the velocity profiles. The simulated results will be compared with the analytical solution (4.10). A symmetric solution with  $z : z = 1 : 1$  (e.g., KCl) are used and the solution has similar physical properties as water at 298 °K:  $\rho \sim 10^3 \text{kg/m}^3$ ,  $\epsilon \sim 6.95 \times 10^{-10} \text{C}^2/\text{J} \cdot \text{m}$ ,  $\mu \sim 10^{-3} \text{N} \cdot \text{s/m}^2$

#### 4.3.1 Effect of the Channel Height to the EDL Thickness Ratio: $\kappa H$

This section presents how the channel height to the EDL thickness ratio  $\kappa H$  will affect the velocity profiles. The ratio  $\kappa H$  can be changed by two methods: one

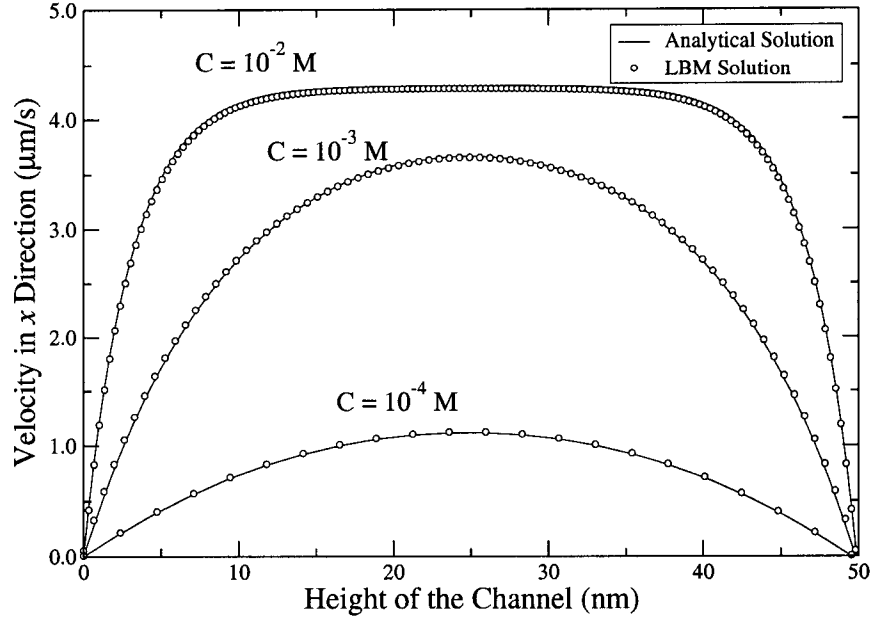


Figure 4.2: Electroosmotic velocity profiles for KCl solution with different ionic molar concentrations  $C$  ( $C = 10^{-2}$  M,  $10^{-3}$  M,  $10^{-4}$  M, channel height  $H = 50$  nm,  $\psi_s = -25$  mV,  $E_x = 250$  V/m).

approach is to change the ionic concentration of the solution while keeping the channel height constant. The EDL thickness will decrease with increasing ionic concentration. The EDL thickness of KCl solution with different ionic molar concentrations are given in Table 3.1. The other method is to change the height of the channels while keeping the ionic concentration constant.

The electroosmosis velocity profiles for different  $\kappa H$  values are plotted in Figures 4.2 and 4.3. The circle represents the results simulated by LBM and the solid line represents the analytical solutions. For each curve in the Figure 4.2, the ionic molar concentration is changed while the same channel height ( $H = 50$  nm), electric potential of the solid surface ( $\psi_s = -25$  mV), and externally applied electric field ( $E_x = 250$  V/m) are constant. The velocity profiles are different from each other because the thickness of the EDL decreases with the increase in the ionic molar concentration. For the solution with a higher

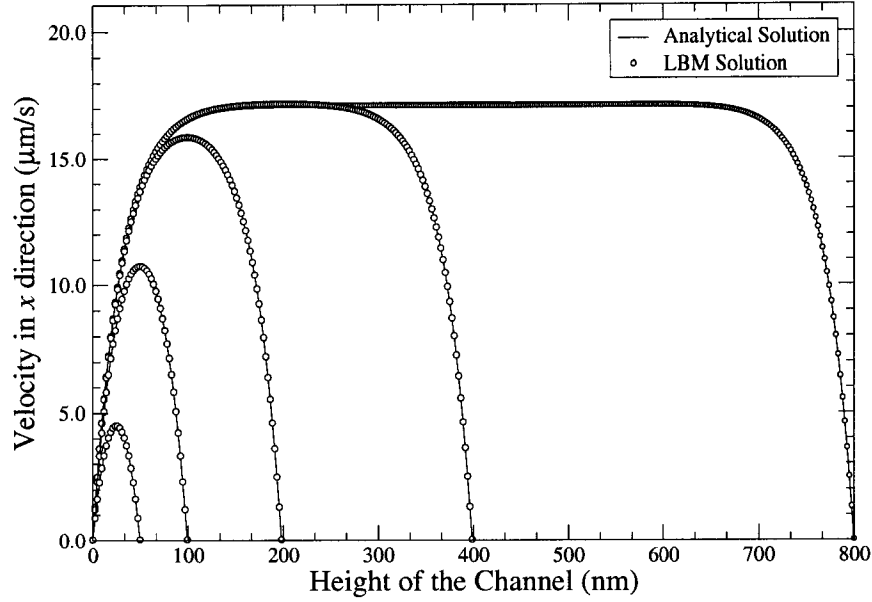


Figure 4.3: Electroosmotic velocity profiles for different channel heights  $H$  ( $H = 50$  nm,  $100$  nm,  $200$  nm,  $400$  nm,  $800$  nm,  $C = 10^{-4}$  M,  $\psi_s = -25$  mV,  $E_x = 1000$  V/m).

ionic molar concentration (e.g.,  $C = 10^{-2}$  M), the ratio of the height and the thickness of the EDL ( $\kappa H = 16$ ) is much larger than 1, suggesting that there is a thin electric double layer. Thus, the fluid moves as a plug under the influence of an electric field along the charged surface. However, for the solution with a lower ionic molar concentration (e.g.,  $C = 10^{-4}$  M),  $\kappa H$  is 1.6, implying a thick electric double layer. Thus, a parabolic velocity profile is obtained due to the large overlap of the double layer with a virtually constant net free charge density across the channel. This gives rise to a fluid body force similar to that of a pressure gradient. In addition, for the flow with a smaller EDL thickness due to a higher ionic concentration, a finer lattice constant  $\delta_x$  is used because a certain number of lattices is required to capture the EDL electrokinetic effect on flow behavior.

For each curve in Figure 4.3, the value of  $\kappa H$  is varied by changing the



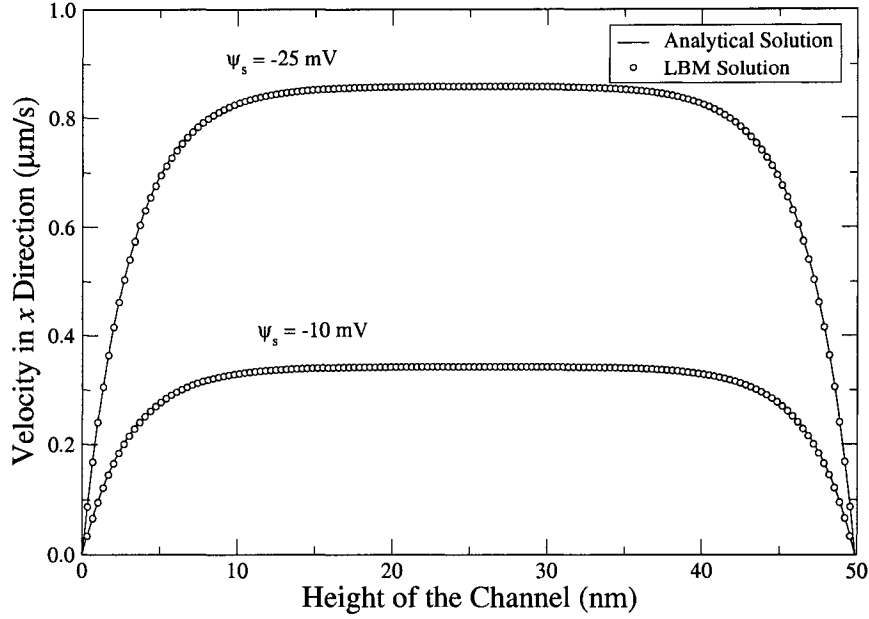


Figure 4.4: Electroosmotic velocity profiles for different surface potential in the same channel ( $H = 50$  nm,  $C = 10^{-2}$  M,  $E_x = 50$  V/m,  $\kappa H = 16$ ).

channel height and keeping other parameters constant. In this simulation, the ionic molar concentration of the solution is  $10^{-4}$  M, so that the lattice constant  $\delta_x$  remains the same for each channel due to the same EDL thickness of 30.4 nm. Both the velocity profile and maximum velocity depend on the height of channels. For example, the velocity profile of the flow with the height of 800 nm is like a plug due to a large  $\kappa H$  value of 27. The maximum velocity for each channel increases with the height  $H$  until  $H = 400$  nm. As can be seen from Figures 4.2 and 4.3, good agreement can be obtained between the simulated and the analytical results.

#### 4.3.2 Effect of Electric Potential of the Solid Surface: $\psi_s$

Here, the surface potential  $\psi_s$  can be controlled and the electroosmotic flow with two different surface potentials:  $\psi_s = -25$  mV and  $-10$  mV are simulated. The

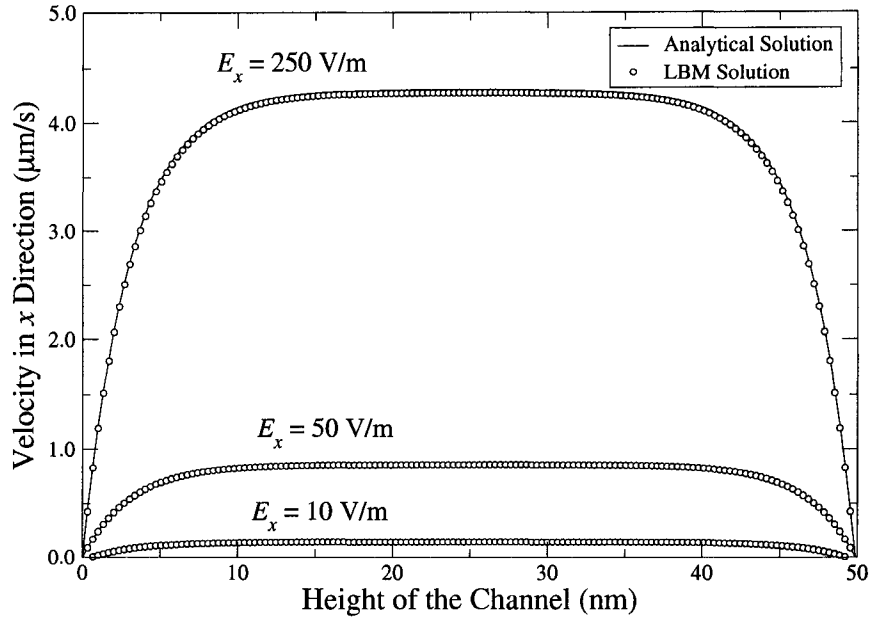


Figure 4.5: Electroosmotic velocity profiles for different externally applied electric field in the same channel ( $H = 50$  nm,  $C = 10^{-2}$  M,  $\psi_s = -25$  mV,  $\kappa H = 16$ ).

ionic molar concentration of the solution is  $10^{-2}$  M and the externally applied electric field  $E_x$  is 50 V/m. From the results shown in Figure 4.4, the simulated results show that higher values for the electric potential of the solid surface will produce a higher flow velocity as expected.

#### 4.3.3 Effect of Externally Applied Electric Field: $E_x$

Electroosmotic flow depends not only on the local net charge density in the fluid but also on the externally applied electric field because the fluid motion is driven by the electrical body force acting on the ions in the diffuse layer of the EDL. Keeping the ionic molar concentration and the surface potential constant, the fluid velocity can be increased by increasing the electric strength  $E_x$ . Figure 4.5 shows the electroosmotic velocity profiles for KCl solution with different externally applied electrical field in the same microchannel. The ionic

concentration is  $10^{-2}$  M and the surface potential  $\psi_s$  is  $-25$  mV. From Figure 4.5, it is obvious that the LBM model prediction matches well with the analytical result.

#### 4.4 Summary

Electroosmotic flow in a straight rectangular microchannel using a D2Q9 Lattice Boltzmann model are simulated. Effects of channel height, surface potential, and applied electric field on the velocity profile were studied and compared with the corresponding analytical solutions. Excellent agreement was found. The LBM model considered here is shown to be an effective computational tool for complex microfluidic systems where an externally applied electric field is imposed.

## CHAPTER 5

# SIMULATION OF ELECTROOSMOTIC FLOW WITH NONUNIFORM ZETA POTENTIAL

### 5.1 Introduction

Microchannel network devices have been widely used in various areas of chemistry and biochemistry. In such microfluidic devices, electroosmosis is often utilized as the tool for fluid transport and mixing simultaneously. The Reynolds number of electroosmotic flow in microfluidic devices is usually very small, and quite often to achieve a sufficient mixing in electroosmotic microchannel flow can be a challenge. Obtaining a complete mixing in either pressure or electric driven microfluidic devices requires both a long mixing channel and an extended retention time to attain a homogeneous solution.

In general, the devices to enhance mixing in microchannel are classified into two categories: passive and active mixer. Complex specific channel geometry is used in passive mixer to increase the interfacial area between the mixing liquids. For example, Liu *et al.* [79] proposed a 3D serpentine channel which enhance mixing via chaotic advection. Strook *et al.* [80, 81] presented a mixing channel with patterned grooves by creating spiral circulation around the flow axis at low

Reynolds number. These methods can achieve complete mixing within a short channel length. However, difficulty remains in the fabrication of complicated geometries for practical application. Compared with passive mixers, active mixers introduce moving parts inside microchannels by applying either an external unsteady pressure perturbation [82] or a sinusoidally alternating electric field [83] to stir the flow stream.

Recently, electroosmotic flow provides an attractive means for controlling fluid motion in microfluidic devices. The characteristics of electroosmotic flow in a microchannel depend on the nature of the surface potential of the channel wall, i.e. whether it is uniform or nonuniform. Most previous studies have focused on electroosmotic flow with uniform surface electric potential  $\psi_s$  [62, 84]. Ajdari [85, 86] investigated electroosmosis with nonuniform surface potential and found circulation regions generated by application of oppositely charged surface heterogeneities to the microchannel wall. The phenomena were also observed experimentally by Strook *et. al.* [64].

From the literature mentioned above, electroosmotic flow with nonuniform surface potential appears to be an excellent alternative to enhance mixing in microfluidics via manipulation of electrical charge distribution in the electric double layer (EDL). It is noted, however, that there is a trade-off between such mixing and flow efficiency and this important factor has often been ignored. That is, excellent mixing could imply poor flow efficiency. Therefore, the purpose of this study is to investigate this trade-off for electroosmotic flow in heterogeneous microchannels by means of the LBM [18–21, 30, 47, 76]. The results from the simulation can be used as guidelines for the optimization and design of microdevices in terms of mixing and species transport.

## 5.2 Description of the Physical System

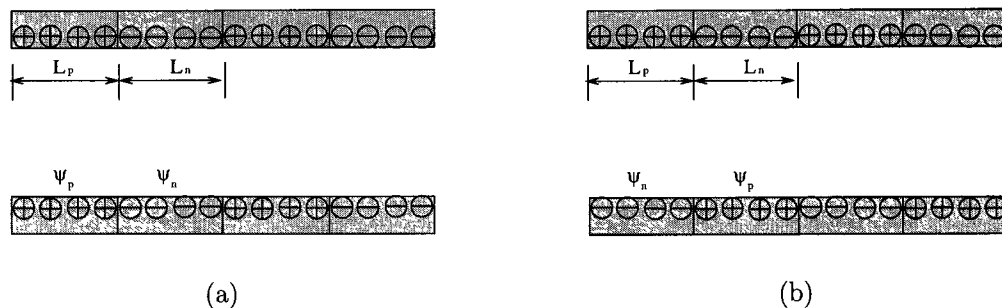


Figure 5.1: Schematic of the patterned surfaces with (a) a symmetric (b) asymmetric stepwise variation of surface potential.  $\psi$  and  $L$  are the surface potential and length of the heterogeneous patches, respectively. The subscripts  $n$  and  $p$  represent the negatively and positively charged surfaces, respectively.

In this chapter, a stepwise surface potential for the heterogeneous microchannel system is employed as shown in Figure 5.1. The microchannel has a width of 500 nm. The patterned surface in Figure 5.1(a) is heterogeneous with symmetrically distributed patches for the lower and upper channel walls; whereas Figure 5.1(b) represents a heterogeneous case where the patches on the lower and upper walls are asymmetric.  $\psi_n$  and  $\psi_p$  are defined as the surface potentials for the negatively and positively charged patches, respectively.

Generally speaking, it is challenging to obtain heterogeneous surface in microchannel via fabrication techniques alone. In practice, there are two methods to achieve a heterogeneous surface. One is to coat the microchannel walls with different materials [64]; the other is to establish an electrical field perpendicular to the microchannel wall via microelectrodes which are embedded inside the solid near the solid-liquid interface [87]. It has been shown that the surface potential can be controlled both spatially and temporally.

## Average Surface Potential

The average surface potential  $\psi_{avg}$  of the channel shown in Figure 5.1 can be calculated from

$$\psi_{avg} = \frac{\psi_p L_p + \psi_n L_n}{L_p + L_n} \quad (5.1)$$

where  $L_p$  and  $L_n$  are the lengths of the positively and negatively charged patches, respectively. In the simulation,  $\psi_n$  is set to be  $-25$  mV while  $\psi_p$  is varied from 0 to 100 mV; the length  $L_n$  and  $L_p$  are also adjusted in terms of the ratio  $L_n/L_p$  to be either 1 or 4.

## Electrical Field

In microchannels with nonuniform surface potential, the governing equations for ion distributions is a two-dimensional problem. The nonlinear Poisson-Boltzmann equation (3.4) becomes

$$\frac{\partial^2 \psi}{\partial x^2} + \frac{\partial^2 \psi}{\partial y^2} = \frac{2n_\infty z e}{\epsilon \epsilon_0} \sinh \left( \frac{z e}{k_b T} \psi \right) \quad (5.2)$$

which can be solved numerically subject to the boundary conditions given by

$$\psi = \psi_1(x) \text{ at } y = 0 \quad \text{and} \quad \psi = \psi_2(x) \text{ at } y = H \quad (5.3)$$

$\psi_1(x)$  and  $\psi_2(x)$  are both function of  $x$  and represent the surface potential at the lower and upper wall, respectively. The net charge density at any point in the channel can be obtained using Eq. (3.3) after the electrical potential distribution  $\psi$  has been found.

The surface potential of microchannel walls can be homogeneous or heterogeneous by implementing  $\psi_1(x)$  and  $\psi_2(x)$  according to real applications. In

this chapter,  $\psi_1(x)$  and  $\psi_2(x)$  are stepwise pattern shown in Figure 5.1. In this model, there are three main assumptions: (1) conductivity is buffer-dominated; that is, it is constant and independent of the local species concentration; (2) charge distribution near the wall is unaffected by an externally applied field; (3) external convective flow does not disturb the EDL distribution. These assumptions are generally valid when the EDL thickness is small, or equivalently, high ionic solution concentration ( $\geq 10^{-4}$  M) and low Reynolds number  $Re$ .

### Flow Field

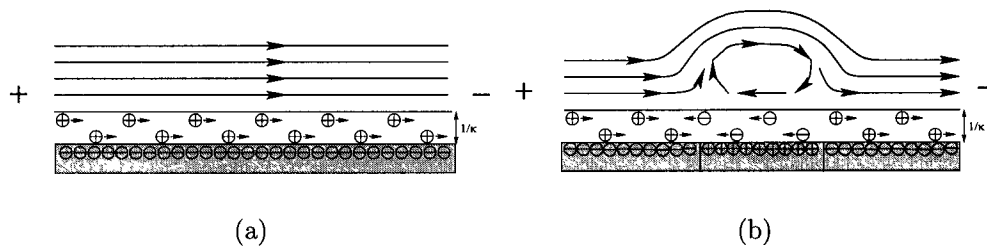


Figure 5.2: Schematic of an electroosmotic flow near the double layer region for (a) a homogeneous surface and (b) a homogeneous surface with a heterogeneous patch.  $1/\kappa$  is the double layer thickness.

The flow field in microchannels with nonuniform surface potential can be obtained numerically rather than analytically. A schematic illustrating how circulation can occur in heterogeneous microchannels is shown in Figure 5.2, where the electric double layer thickness is shown as  $1/\kappa$ . In Figure 5.2(a), an electroosmotically driven flow over a homogeneous surface with a surface potential  $\psi = -\psi_0$  ( $\psi_0 > 0$ ) is presented. The excess positive ions of the electric double layer (EDL) are driven by the electroosmotic body force when an external electric field (negative downstream) is applied across two ends of the microchannel. This drags the bulk fluid due to viscous effect. The same effect



also happens for a heterogeneous surface with a step change nonuniform surface potential shown in Figure 5.2(b); in this case, the electroosmotic body force is applied to both regions of excess negative and positive ions. As a result, the flow near the positively charge patch with  $\psi = \psi_0$  ( $\psi_0 > 0$ ) is in the opposite direction to that of the homogeneous regions ( $\psi = -\psi_0$ ). The interaction of these local flow fields with the bulk results in regional circulation zone as shown in Figure 5.2(b) [64, 85, 86].

### 5.3 Results and Discussion

#### 5.3.1 Influence of the Nonuniform Surface Potential on the Velocity Profiles

The simulation results are presented here for a 1 : 1 electrolyte with an ionic molar concentration of  $10^{-4}$  M having an EDL thickness of 30.4 nm. The externally applied electric field was set to be 1000 V/m for the following 4 cases.

##### 1. Symmetric with $L_n/L_p = 1$

The surface potentials  $\psi_p$  are set to vary from 0 to 25 mV in a 5 mV increment while  $\psi_n$  remains a constant value of  $-25$  mV for  $L_n/L_p = 1$ . Figure 5.3(a)–(c) shows a series of velocity field generated by modeling the heterogeneous surface with symmetrically distributed patches; symmetric implies that the surface potentials on the upper and lower walls are exactly the same in terms of both magnitude and sign. As expected, the flow fields presented in these figures exhibit local circulations near the heterogeneous region with a positive surface potential. No circulation was found in Figure 5.3(a) when  $\psi_p = 0$  mV. The largest circulation results from setting  $\psi_p = |\psi_n|$  in Figure 5.3(c) where the average surface potential  $\psi_{avg}$  is zero. From Figure 5.3(c), the sizes of the vortex

appear to be the same when  $\psi_p = |\psi_n| = 25$  mV. It was found that the absolute values of the maximum velocities in each vortex are the same. The flow fields for  $\psi_p = 5, 10$  and  $15$  mV are similar to that shown in Figure 5.3(b) and not shown.

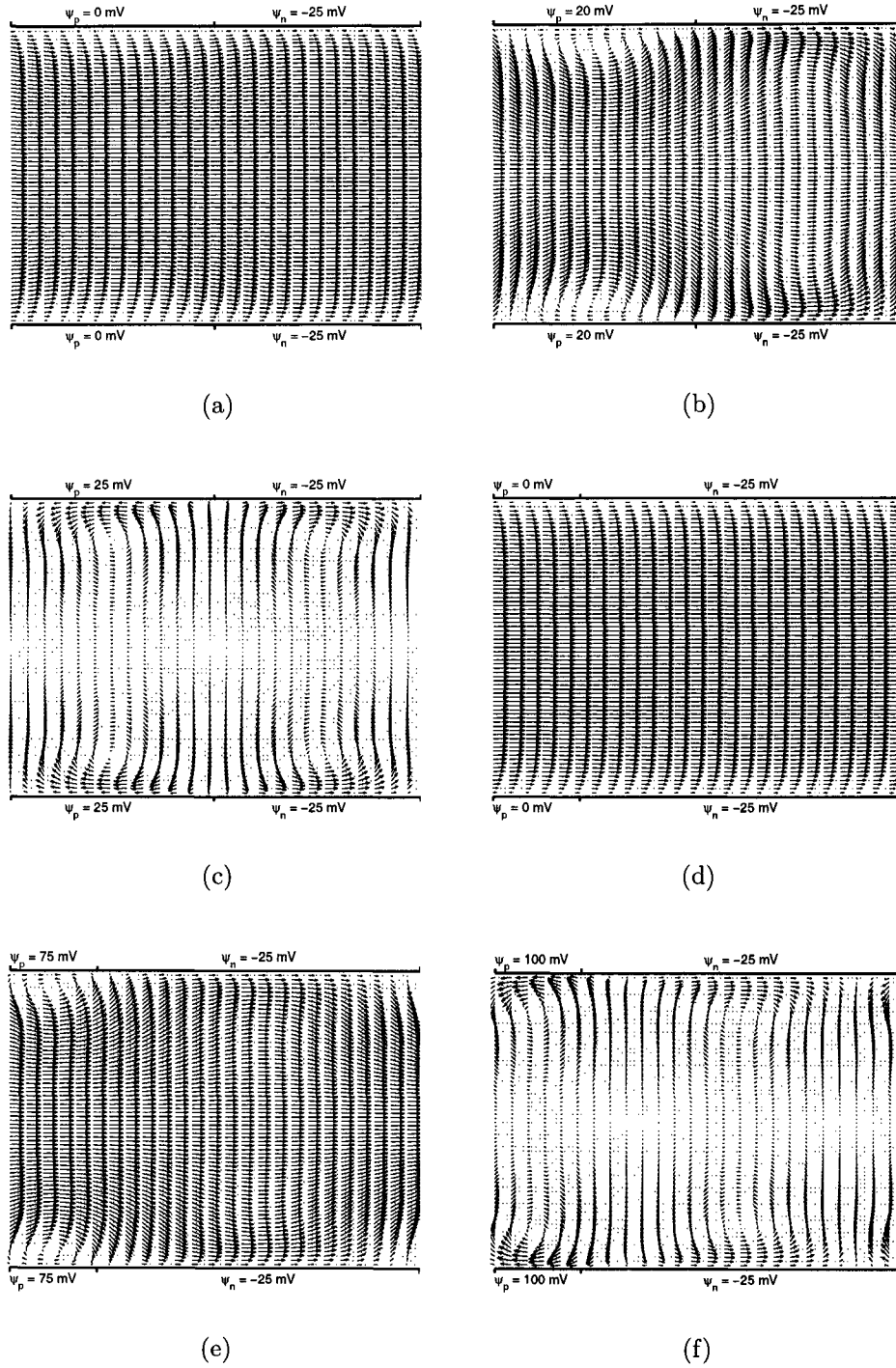


Figure 5.3: Velocity profiles for a symmetrically arranged nonuniform surface potential when  $\psi_n = -25$  mV and (a)  $\psi_p = 0$  mV and  $L_n/L_p = 1$ ; (b)  $\psi_p = 20$  mV and  $L_n/L_p = 1$ ; (c)  $\psi_p = 25$  mV and  $L_n/L_p = 1$ ; (d)  $\psi_p = 0$  mV and  $L_n/L_p = 4$ ; (e)  $\psi_p = 75$  mV and  $L_n/L_p = 4$ ; (f)  $\psi_p = 100$  mV and  $L_n/L_p = 4$ .

## 2. Symmetric with $L_n/L_p = 4$

Here, the ratio of  $L_n/L_p$  is set to be 4 while  $\psi_p$  varies from 0 to 100 mV in a 25 mV increment while  $\psi_n$  remains a constant value of  $-25$  mV. As shown in Figure 5.3(d)–(f), the magnitude of the circulation increases as  $\psi_p$  increases from 0 mV (Figure 5.3(d)) to 100 mV (Figure 5.3(f)). Contrary to the results in Figure 5.3(c), the sizes of the vortex in Figure 5.3(f) are not the same for a different  $L_n/L_p$  ratio; that is, the larger the dimension  $L_n$ , the larger is the circulation size. However, the absolute value of the maximum velocity, in the region where  $\psi$  is positive ( $\psi_p$ ), is larger than that with a negative  $\psi$  value ( $\psi_n$ ). Thus, the patterns of the flow fields are dramatically different due to the magnitude and size of the positively charged heterogeneous regions. The circulation regions expands as the magnitude of the heterogeneous surface potential  $\psi_p$  increases. These expanded circulation regions force the bulk to flow through a narrower channel cross section [cf. Figures 5.3(c) and 5.3(f)], resulting in a shorter local diffusion length which enhances mixing.

## 3. Asymmetric with $L_n/L_p = 1$

This section is similar to those studied above, except that the heterogeneous patches here are arranged asymmetrically for the upper and lower channel walls. The velocity field generated from the asymmetric heterogeneous surfaces are shown in Figure 5.4(a)–(c) where  $\psi_p$  increases from 0 to 25 mV in a 5 mV increment while  $\psi_n$  is set to be a constant value of  $-25$  mV. Other flow fields with  $\psi_p = 5, 10$  and  $15$  mV are not shown. Similar to the symmetric case given above, local circulation region can be obtained near the heterogeneous patch with a positive surface potential  $\psi_p$ . The different sizes of circulation regions are due to both the magnitude ( $\psi_p$ ) and dimension ( $L_p$ ) of the heterogeneous patches. It is also apparent that the flow field patterns are different from the

symmetric case above. Compared to the flow fields in Figures 5.3(c) and 5.4(c), the direction of the vortex has changed as a result of rearrangement (whether symmetric or asymmetric) of the heterogeneous patches.

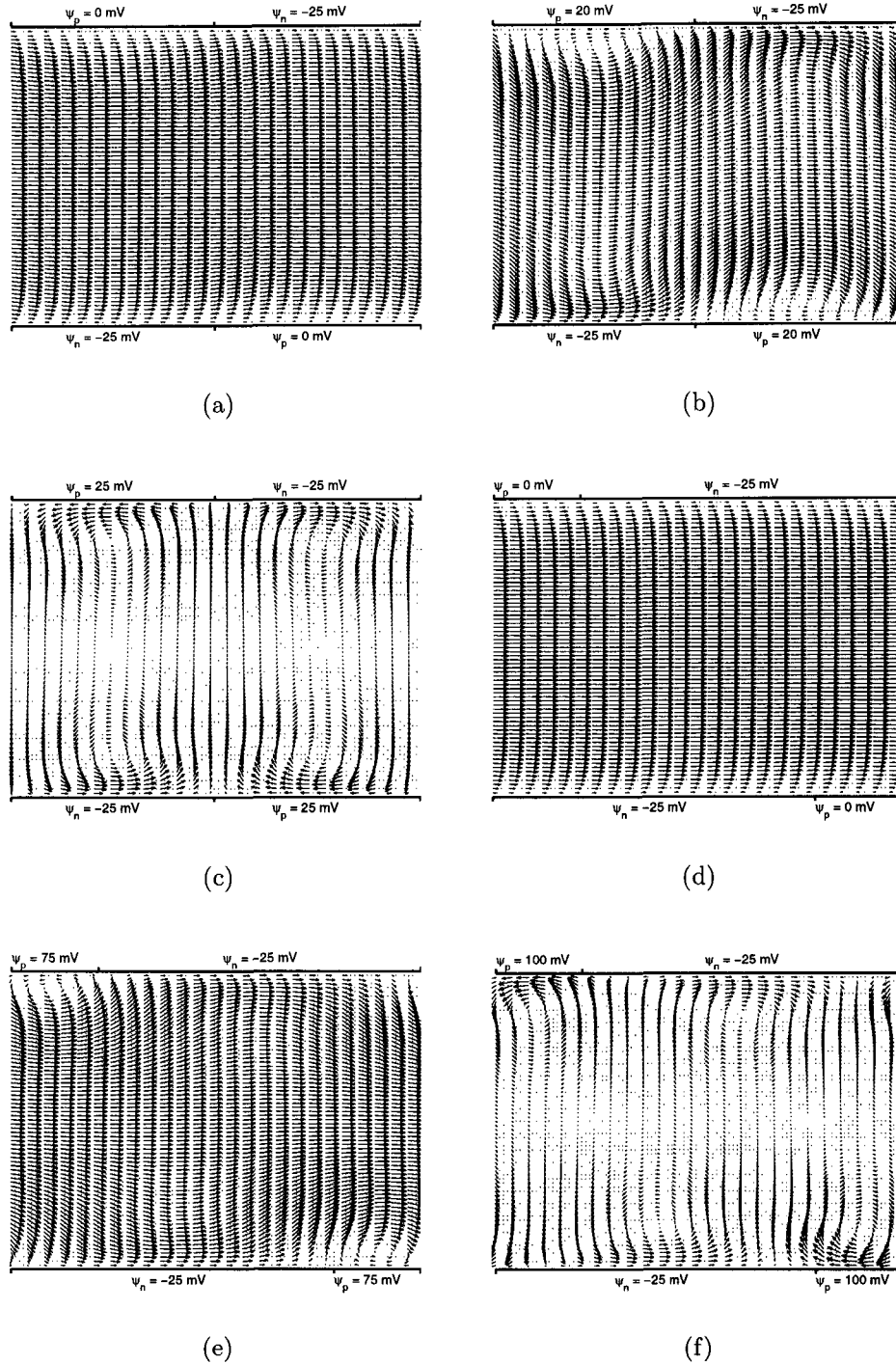


Figure 5.4: Velocity profiles for an asymmetrically arranged nonuniform surface potential when  $\psi_n = -25$  mV and (a)  $\psi_p = 0$  mV and  $L_n/L_p = 1$ ; (b)  $\psi_p = 20$  mV and  $L_n/L_p = 1$ ; (c)  $\psi_p = 25$  mV and  $L_n/L_p = 1$ ; (d)  $\psi_p = 0$  mV and  $L_n/L_p = 4$ ; (e)  $\psi_p = 75$  mV and  $L_n/L_p = 4$ ; (f)  $\psi_p = 100$  mV and  $L_n/L_p = 4$ .

#### 4. Asymmetric with $L_n/L_p = 4$

The ratio of  $L_n/L_p$  is set to 4 here for an asymmetric arrangement of the heterogeneous patches. The simulation was based on  $\psi_n = -25$  mV while  $\psi_p$  increases from 0 to 100 mV in a 25 mV increment; the results are shown in Figure 5.4(d)–(f), where the circulation magnitude increases from zero (Figure 5.4(d)) to the largest in Figure 5.4(f) when  $\psi_p$  is 100 mV (i.e.,  $\psi_{avg} = 0$  mV). The flow field in Figure 5.4(f) shows that the sizes of the vortex are not same when  $L_n \neq L_p$ ; that is, the larger the dimension  $L_n$ , the bigger is the circulation size. However, the absolute value of the maximum velocity in the  $\psi_p$  region is larger than that of the  $\psi_n$  region. Because of the asymmetric distribution and dimension of the charged patches, the flow field in Figure 5.4(f) is the most tortuous. For example, the bulk flow in Figure 5.3(b) and 5.3(e) are forced to converge into a narrow stream by the symmetric circulation region while the flow fields shown in Figures 5.4(b) and 5.4(e) are more tortuous as a result of the offset, asymmetric circulation region. In addition, movement perpendicular to the applied field can be generated in the circulation regions by comparing Figures 5.3(c), 5.3(f), 5.4(c) and 5.4(f). Such kind of motion could be particularly useful in system mixing. On the other hand, near the junction of positively and negatively charged regions is a stagnation point which may be useful for manipulation of macromolecules or cells in a fluid environment.

### 5.3.2 Influence of the Nonuniform Surface Potential on the Volumetric Flow Rate

According to the mass continuity condition, the volumetric flow rate at any cross section of the channel are the same and can be calculated by

$$Q = \int u(y, z)W dydz \quad (5.4)$$

where  $Q$  is the volumetric flow rate,  $u(y, z)$  is the local velocity in the  $x$  direction. For a 2D simulation, Eq.(5.4) can be simplified as the velocity  $u$  and is independent of the width  $z$ . In order to study the systematic effect of  $\psi_p$  on the volumetric flow rate,  $Q$  is normalized by the maximum flow rate  $Q_{max}$ , i.e., the flow rate of the same channel having a uniform surface potential of  $\psi = -25$  mV. As discussed before, it is anticipated that nonuniform surface potential affects not only the flow field but also the flow rate for liquid transport. The dependence of electroosmotic flow rate on the nonuniform surface potential is illustrated below:

#### 1. Effect of $\psi_p$ on $Q/Q_{max}$

The effect of  $\psi_p$  on the normalized flow rate  $Q/Q_{max}$  is shown in Figure 5.5 using the results discussed above. In Figure 5.5, filled diamonds and squares represent the normalized volumetric flow rate versus the values of  $\psi_p$  for symmetrically distributed charged patches; while circles and triangles represent similar results for asymmetrically arranged patches. The normalized flow rates  $Q/Q_{max}$  for  $L_n/L_p = 4$  (as  $\psi_p$  increases from 0 to 100 mV in a 25 mV increment) are shown as curve A. Those of  $L_n/L_p = 1$  (as  $\psi_p$  increases from 0 to 25 mV in a 5 mV increment) are shown as curve B. From this figure,  $Q/Q_{max}$  decreases linearly as  $\psi_p$  increases for both curves A and B. From each line, it is concluded



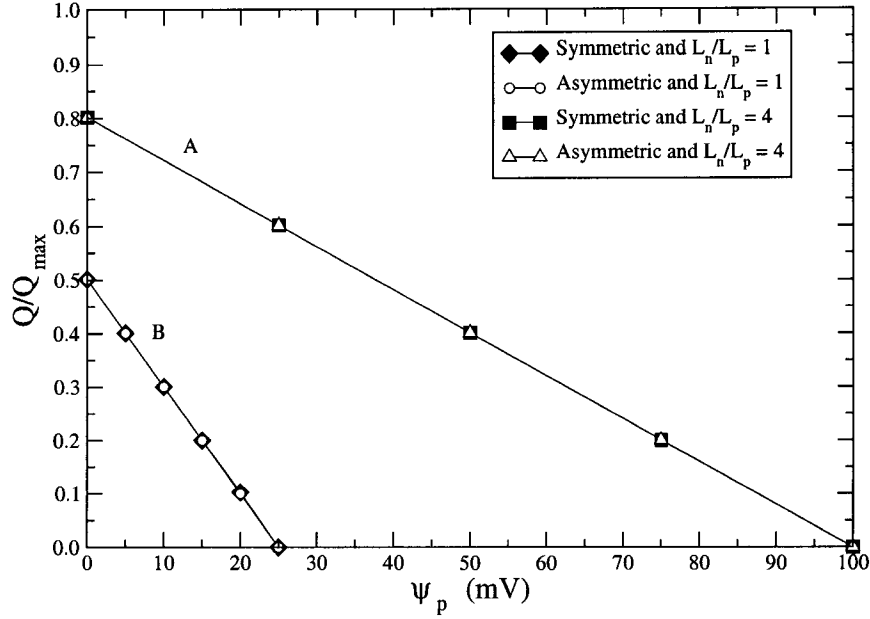


Figure 5.5: Normalized volumetric flow rate versus surface potential of the positively charged region  $\psi_p$  when  $\psi_n = -25$  mV. Curve A represents the case of  $L_n/L_p = 4$  and  $\psi_p = 0, 25, 50, 75,$  and  $100$  mV; Curve B represents the case of  $L_n/L_p = 1$  and  $\psi_p = 0, 5, 10, 15, 20,$  and  $25$  mV.

that arrangement of nonuniform surface potential, i.e. either symmetric or asymmetric, does not affect this linear relation. Comparing with curves A and B shows that for the same surface potential  $\psi_p$ ,  $Q/Q_{max}$  for  $L_n/L_p = 1$  is smaller than that when  $L_n/L_p = 4$ .

## 2. Effect of $L_p/(L_p + L_n)$ on $Q/Q_{max}$

Using the previous simulation results, Figure 5.6 shows that the dependence of the normalized flow rate  $Q/Q_{max}$  on the ratio  $R = L_p/(L_n + L_p)$ . These results were obtained by adjusting  $L_p$  for  $R = 0, 0.2, 0.4$  and  $0.5$  while the values of  $\psi_n$ ,  $\psi_p$  and  $L_n$  are set to be constant. In Figure 5.6, the circles and filled squares represent the normalized volumetric flow rate versus the length of the positively charged region  $L_p$  in the microchannel with symmetrically and asymmetrically distributed charged patches, respectively. It is again apparent that  $Q/Q_{max}$

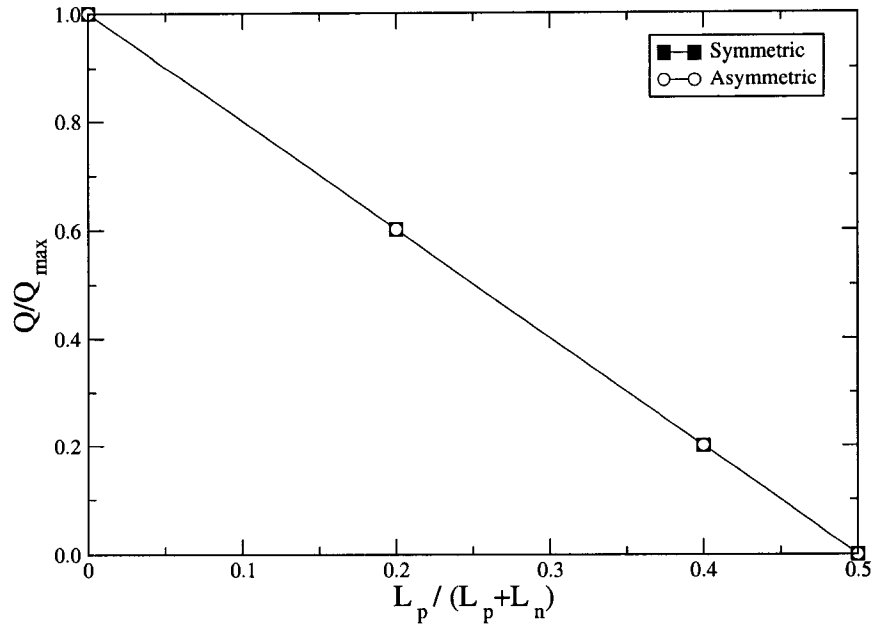


Figure 5.6: Normalized volumetric flow rate versus length ratio of the positively charged region  $L_p/(L_p + L_n)$  for  $\psi_p = |\psi_n| = 25$  mV.

decreases linearly as the ratio  $L_p/(L_p + L_n)$  increases for both symmetric and asymmetric cases. Thus, arrangement of the nonuniform surface potential, i.e. symmetric or asymmetric, will have no effect on the normalized flow rate.

It is then instructive to study how the normalized flow rate  $Q/Q_{max}$  changes with the heterogeneous surface potentials. From Eq.(5.1), an average surface potential  $\psi_{avg}$  has been defined and can be calculated in terms of both the magnitude of the surface potential  $\psi_p$  and length  $L_p$  of the heterogeneous patch. Figure 5.7 shows the results for the normalized flow rate with the average surface potential, using the data from Figures 5.5 and 5.6. The normalized flow rate  $Q/Q_{max}$  indeed depends only on the average surface potential  $\psi_{avg}$  even though the individual flow field could have been different. That is to say, once an average surface potential is known, the normalized flow rate remains the same and does not depend on the heterogeneous pattern of the surface. Therefore,

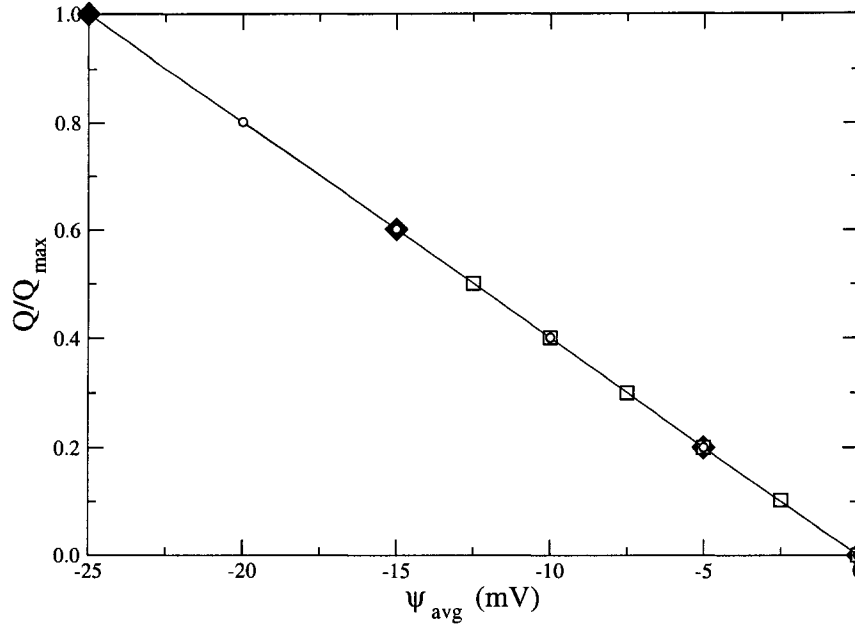


Figure 5.7: Normalized volumetric flow rate versus average surface potential  $\psi_{avg}$  when  $\psi_n = -25$  mV and  $\square$ :  $L_n/L_p = 1$  and  $\psi_p = 0, 5, 10, 15, 20,$  and  $25$  mV;  $\blacklozenge$ :  $\psi_p = 25$  mV and  $L_p/(L_p + L_n) = 0, 0.2, 0.4,$  and  $0.5$ ;  $\circ$ :  $L_n/L_p = 4$  and  $\psi_p = 0, 25, 50, 75,$  and  $100$  mV.

it is safe to conclude that arrangement of nonuniform surface potential, i.e. symmetric or asymmetric, has no affect on the flow rate and the average surface potential defined in Eq.(5.1) is a means by which electroosmotic flow rate can be evaluated in a microchannel with nonuniform surface potentials.

### 5.3.3 Trade-off between Mixing and Flow Efficiency of Microfluidics with Heterogeneous Surfaces

According to results in Figures 5.3 and 5.4, the complex pattern of the heterogeneous surface potential will enhance mixing due to circulation and tortuosity and should result in a higher mixing efficiency. In order to obtain larger circulation and tortuosity, the average surface potential  $\psi_{avg}$  calculated by Eq. (5.1) should be as close to zero as possible. However, from the flow rate discussion

above in Figure 5.7, as  $\psi_{avg}$  approaches zero, the normalized flow rate  $Q/Q_{max}$  also decreases to zero. Indeed, there is a trade-off between the mixing efficiency and flow efficiency via circulation induced by heterogeneous surface potential. Thus, design and applications of such phenomena for mixing should be carefully considered. On the one hand, mixing is required; on the other, liquid transport is also an important issue for electroosmotic flow.

#### 5.4 Summary

In this chapter, the LBM with the Poisson-Boltzmann equation has been used to simulate electroosmotic flow in a  $0.5 \mu\text{m}$  microchannel with heterogeneous surface potential. The simulation results indicate that local circulations can be obtained near the heterogeneous region, in agreement with those obtained by other authors using traditional CFD method. Different patterns of the heterogeneous surface potential cause different magnitude of the circulation. The largest circulation, which implies the highest mixing efficiency due to convection and short-range diffusion, was found when the average surface potential is zero. A zero average surface potential, however, implies zero flow rate. It has been shown that there is a clear trade-off between the mixing efficiency and flow efficiency in microfluidics with heterogeneous surfaces.

## CHAPTER 6

# SIMULATION OF ELECTROKINETIC FLOWS WITH CONSTRAINTS OF CURRENT CONTINUITY

### 6.1 Introduction

Pressure-driven flow and electroosmotic flow are two main methods in most microfluidics applications. These flows are usually laminar due to the low Reynolds number. For electrokinetic flows in microchannels with homogeneous surface potential, analytical solutions are available in cylindrical capillaries [88, 89], slit channel [90], and straight rectangular microchannels [91, 92]. If the surface potentials of these channels are heterogeneous, the electrokinetic problems have to be solved numerically and the characteristics of the flow would depend on both the pattern of the surface potential (i.e. whether the surface charge is a step or continuous change) and the potential distribution along the channel. For electroosmotic flows, the flow field could be changed from laminar to multidirection with circulation as discussed in the chapter 5 [64, 85, 86]. However, in most of such models, current continuity across sections of non-uniform microchannels is not automatically satisfied. Until recently, Yang et al. [93] proposed a model to describe the behavior in circular microchannels with nonuniform surface poten-

tials where the continuities of flow rate and electrical current were considered simultaneously by solving the modified Navier-Stokes and Poisson-Boltzmann equations.

In this chapter, the LBM is employed to simulate electrokinetic flows with step change surface potentials by considering both flow rate and current continuities. The continuity of flow rate is satisfied automatically in the LBM scheme. From the simulation results, a step change potential distribution along the channel and a reduced flow rate due to the constraint of current continuity for a step change potential distribution along a channel in both pressure-driven and electroosmotic flow are obtained. The results indicate that step change in surface potential and hence ion distribution influence significantly the electrical potential distribution along the channel, velocity profiles and volumetric flow rate.

## **6.2 Description of the Physical System**

### **Electric Field**

In this chapter, the geometry of the channel with step-changing surface potential is shown in Figure 6.1. The electric field and the ion distribution can be obtained by numerically solving the nonlinear Poisson-Boltzmann equation (5.2) subject to the same boundary conditions as that (Eqs. (5.3)) in Chapter 5. The potential distribution along the channels can be evaluated through the solution of Laplace Eq. (4.2).

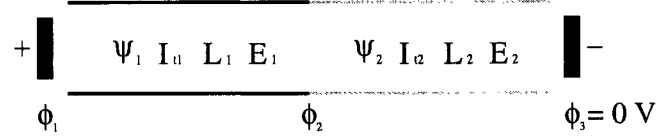


Figure 6.1: Geometry of a 2D heterogeneous microchannel, consisting of two different sections.  $\psi_1$  and  $\psi_2$  are the two stepwise variation of surface potentials for the heterogeneous channel.

### Constraints of Current Continuity

**Pressure-Driven Flow** For steady-state pressure-driven electrokinetic flow in nano and microchannels, the total electric current  $I_t$  defined by Eq. (3.8) in Chapter 3 should be zero so that the constraint of current continuity on the flow system is

$$I_t = 0 \quad (6.1)$$

Once the flow field is known, the convection current or the streaming current will be evaluated by Eq. (3.9). Combining Eqs. (3.10) and (6.1), the streaming potential can be determined from

$$\phi = -L \frac{\int_0^H u_x(x, y) \rho_e(x, y) dy}{(\lambda_b + \lambda_s \frac{P_w}{A_c}) H} \quad (6.2)$$

The conduction current can be obtained by Eq. (3.10) or (3.11). The strength of the induced electric field  $E$  is  $\frac{\phi}{L}$ . As the induced streaming potential will produce an electroosmotic effect, an additional body force caused by the streaming potential acting on the EDL will be applied to the LBM equation as well as pressure body force; the velocity will then be recalculated in order to obtain a more accurate streaming potential.

**Electroosmotic Flow** In electroosmotic flow, the total current  $I_t$  can be calculated by substituting Eqs. (3.9) and (3.10) into Eq. (3.8) in Chapter 3. For the heterogeneous nano and microchannel with nonuniform surface potential ( $\psi_1$  and  $\psi_2$ ) represented as two sections in Figure 6.1, the constraint of current continuity is  $I_{t1} = I_{t2}$  and hence

$$\begin{aligned}
I_{t1} &= \int_0^H u_{x1}(x, y) \rho_{e1}(x, y) W dy + A_c \lambda_b E_1 + P_w \lambda_{s1} E_1 \\
&= \int_0^H u_{x2}(x, y) \rho_{e2}(x, y) W dy + A_c \lambda_b E_2 + P_w \lambda_{s2} E_2 \\
&= I_{t2} \\
E_1 &= \frac{\phi_1 - \phi_2}{L_1} \\
E_2 &= \frac{\phi_2 - \phi_3}{L_2}
\end{aligned} \tag{6.3}$$

Subscripts 1 and 2 represent the properties to the left and right sections in Figure 6.1, respectively. By considering this constraint, the electric potential  $\phi_2$  at the junction between the two different surface potentials ( $\psi_1$  and  $\psi_2$ ) can be evaluated according to the velocity profile and externally applied electric potential  $\phi_1$  when  $\phi_3 = 0$  V. For instance, if the surface potential of the left section is set to be zero  $\psi_1 = 0$  (i.e. no EDL effect), the net charge  $\rho_{e1}$  and surface conductivity  $\lambda_{s1}$  are zero, Eq. (6.3) can be simplified to

$$\begin{aligned}
I_{t1} &= A_c \lambda_b E_1 \\
&= \int_0^H u_{x2}(x, y) \rho_{e2}(x, y) W dy + A_c \lambda_b E_2 + P_w \lambda_{s2} E_2 \\
&= I_{t2} \\
E_1 &= \frac{\phi_1 - \phi_2}{L_1} \\
E_2 &= \frac{\phi_2}{L_2}
\end{aligned} \tag{6.4}$$



In this case,  $\phi_2$  can be calculated by

$$\phi_2 = \frac{\frac{A_c \lambda_b \phi_1}{L_1} - \int_0^H u_{x2}(x, y) \rho_{e2}(x, y) W dy}{\frac{A_c \lambda_b}{L_1} + \frac{A_c \lambda_b}{L_2} + \frac{P_w \lambda_{s2}}{L_2}} \quad (6.5)$$

### 6.3 Results and Discussion

As mentioned earlier, the purpose of this study is to investigate the effect of nonuniform surface potential on the potential distribution along the channel and volumetric flow rate by considering the current continuity using the LBM in which the continuity of flow rate is satisfied automatically. A stepwise variation of surface potential is selected and shown in Figure 6.1 where  $\psi_1$  and  $\psi_2$  are the surface potentials of the left and right sections with a length of  $L_1$  and  $L_2$ , respectively. A symmetric electrolyte solution (KCl) with  $z : z = 1 : 1$  was employed and its physical properties are similar to those of water at 298°K:  $\rho \sim 10^3 \text{ kg/m}^3$ ,  $\epsilon \sim 6.95 \times 10^{-10} \text{ C}^2/\text{J}\cdot\text{m}$ , and  $\mu \sim 10^{-3} \text{ N}\cdot\text{s/m}^2$ . The bulk conductivity  $\lambda_b$  of the solution is  $1.42 \times 10^{-3} \text{ S/m}$  and the surface conductivity  $\lambda_s$  is 1.64 nS [94]. In this simulation, the variation of the surface potential is assumed not to influence the bulk and surface conductance for the KCl electrolyte solution. The ionic molar concentration of solution is set to be  $10^{-4} \text{ M}$  with a EDL thickness  $1/\kappa$  of 30.4 nm. The height of the channel  $H$  is assumed to be 500 nm for  $\kappa H = 16$ . At this ratio, the EDL will not overlap and a plug-like electroosmotic flow can be obtained.

#### 6.3.1 Pressure-Driven Flow

It is well-known that a streaming potential sets up when a liquid is forced through a microchannel under an applied pressure gradient. The streaming

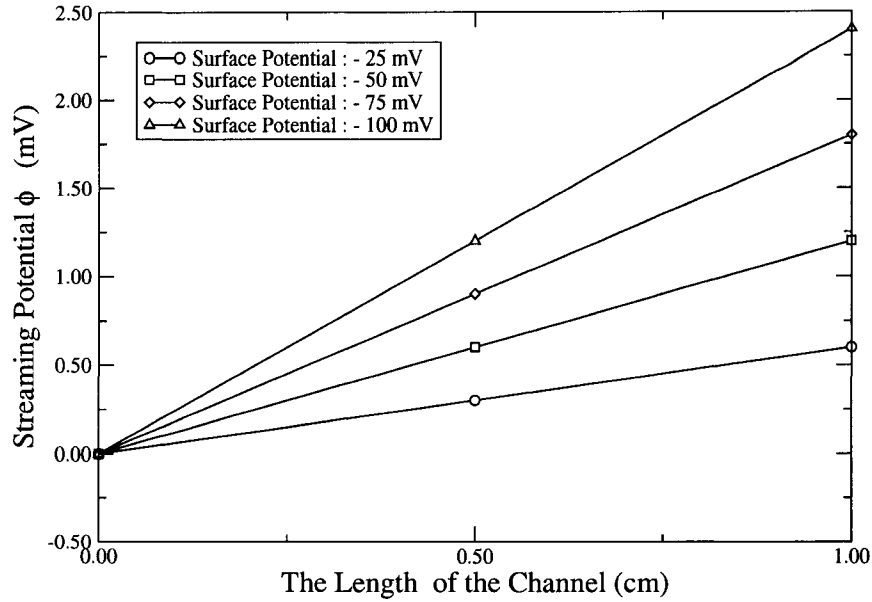


Figure 6.2: Streaming potential along a 1 cm rectangular microchannel ( $H = 500$  nm) with a uniform surface potential for  $\psi = -25$  to  $-100$  mV, in a 25 mV increment. The pressure gradient is  $dP/dx = 10$  MPa/m.

potential can be obtained by considering the constraint of current continuity as shown in Eq. (6.1). For a channel with uniform surface potential, the streaming potential is proportional to the surface potential and the distribution along the channel is linear as shown in Figure 6.2 for  $\psi = -25$  to  $-100$  mV, in a 25 mV increment.

For a channel with nonuniform surface potential such as a stepwise variation of surface potential, the streaming potential  $\phi$  will be different. In the simulation, the surface potential of the section to the left  $\psi_1$  in Figure 6.1 is set as 0 while that of the right  $\psi_2$  to be negatively charged. The junction of two sections is at the mid-point of the channel having a length of 1.0 cm ( $L = 2L_1 = 2L_2$ ). The convection current  $I_s$  in the left section will be zero because of zero net charge in the solution due to no EDL, so that the streaming potential is also zero. For the section to the right, a streaming potential will be set up

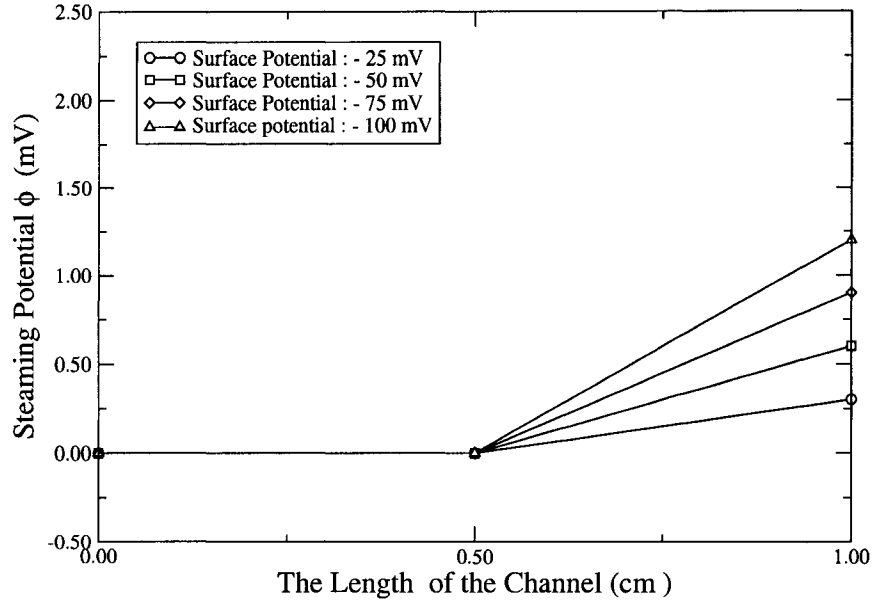


Figure 6.3: Streaming potential along a 1 cm rectangular microchannel ( $H = 500$  nm) with a nonuniform surface potential for  $\psi_2 = -25$  to  $-100$  mV, in a 25 mV increment. The pressure gradient is  $dP/dx = 10$  MPa/m.

and the results are presented in Figure 6.3 for  $\psi_2 = -25$  to  $-100$  mV, in a 25 mV increment. This result indicates that streaming potential relates to the surface potential and ion distribution associated with the surface potential, in agreement with intuition.

### 6.3.2 Electroosmotic Flow

The constraint of current continuity is, however, not apparent in electroosmotic flow. In this section, the volumetric flow rate and potential distribution for electroosmotic flow in a channel are calculated with a stepwise variation of surface potential. The constraint of current continuity is also considered and the results are compared against those without such a constraint. The externally applied potentials are set  $\phi_1 = 100$  V at the inlet and  $\phi_3 = 0$  V at the outlet. The surface potential of the left section  $\psi_1$  in Figure 6.1 is set to 0 while that

of the right  $\psi_1$  to be negatively charged.

### Potential Distribution along the Channel

For a channel with a uniform surface potential, the electric potential distribution along the channel governed by the Laplace equation (4.2) is linear and the electric field strength  $E$  is constant based on the assumptions of a thin EDL and constant permittivity  $\epsilon$ . Thus, the potential  $\phi_2$  at the junction equals  $\frac{\phi_1 - \phi_3}{2}$  and hence  $\phi_2 = 50$  mV. When the surface potential is nonuniform such as that shown in Figure 6.1, the potential distribution along the channel depends whether or not current continuity is considered. If the constraint of current continuity  $I_{t1} = I_{t2}$  is not involved, the potential distribution is usually regarded as identical to the case with a uniform surface potential, i.e.,  $\phi_2 = \frac{\phi_1 - \phi_3}{2}$ . However, the realistic situation is that current continuity should also be considered in electroosmotic flow for nonuniform surface potential and the potential distribution along the channel between  $\phi_1$  and  $\phi_3$  will not be linear. For a stepwise variation in surface potential, there is a step change in the potential distribution as given in Figure 6.4. As can be seen from this figure, the potential at junction  $\phi_2$  becomes 15 mV, rather than 50 mV. This represents a 70% (35 mV) decrease from the linear assumption [ $\phi_2 = (100 - 0)/2 = 50$  mV] when the constraint of current continuity is considered.

The above phenomenon can be explained by the analogy of an equivalent electrical circuit shown in Figure 6.5. In this circuit, the conductance  $\lambda_1$  and  $\lambda_2$  correspond to the conductance for the left and right sections in Figure 6.1, respectively. Compared to the electroosmotic system mentioned earlier,  $\lambda_1 = \lambda_b$  and  $\lambda_2$  is the sum of the bulk conductance  $\lambda_b$ , surface conductance  $\lambda_s$  and the equivalent conductance due to convective current  $I_s$ . Obviously, the value

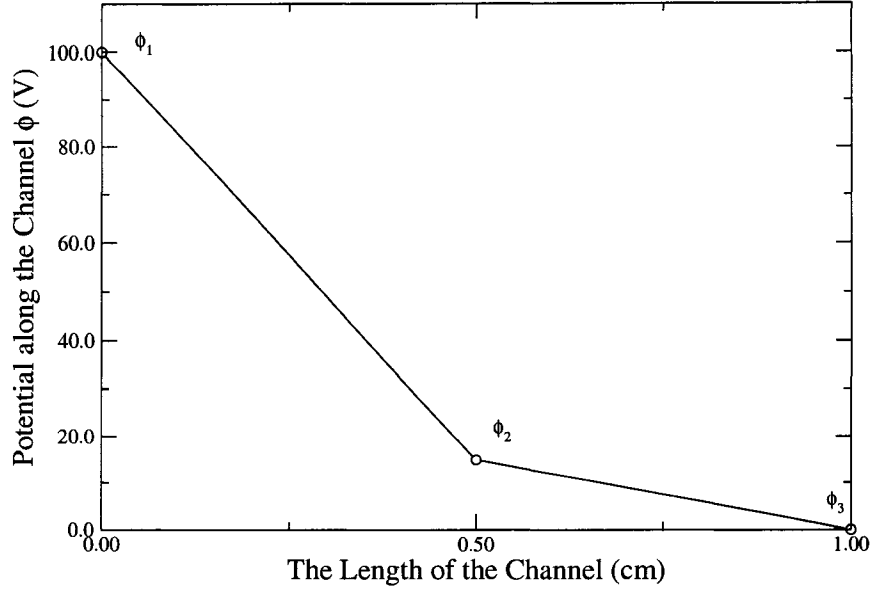


Figure 6.4: Distribution of potential along a 1 cm rectangular microchannel ( $H = 500$  nm) with a stepwise variation of surface potential ( $\psi_1 = 0$  mV and  $\psi_2 = -5$  mV.) when the constraint of current continuity is considered in electroosmotic flow

of  $\lambda_1$  is smaller than  $\lambda_2$ . Thus, the resistance  $R_1$  should be higher than  $R_2$ . According to Ohm's law and the current continuity  $I_1 = I_2$  in a series circuit,  $\frac{\phi_1 - \phi_2}{R_1} = \frac{\phi_2 - \phi_3}{R_2}$  can be obtained so that the  $\phi_2$  for  $R_1 > R_2$  should be smaller than that for  $R_1 = R_2$ , given that the  $\phi_1$  and  $\phi_3$  are fixed at the same value. This analogy applies to the electroosmotic system when nonuniform surface potential and current continuity are involved; the potential  $\phi_2$  at the junction between the two heterogeneous sections will decrease significantly from the case with uniform surface potential or without current constraint. Nevertheless, the potential distribution in each section remains linear as shown in Figure 6.4.

Figure 6.6 presents the ratio of the potential  $\phi_2/\phi_1$  for different surface potentials  $\psi_2$  of the section on the right. The potential  $\phi_2$  is normalized by the potential  $\phi_1$  at the inlet. From this figure, the potential  $\phi_2/\phi_1$  or  $\phi_2$  increases nonlinearly with the surface potential  $\psi_1$ . The variation of the potential  $\Delta\phi_2$

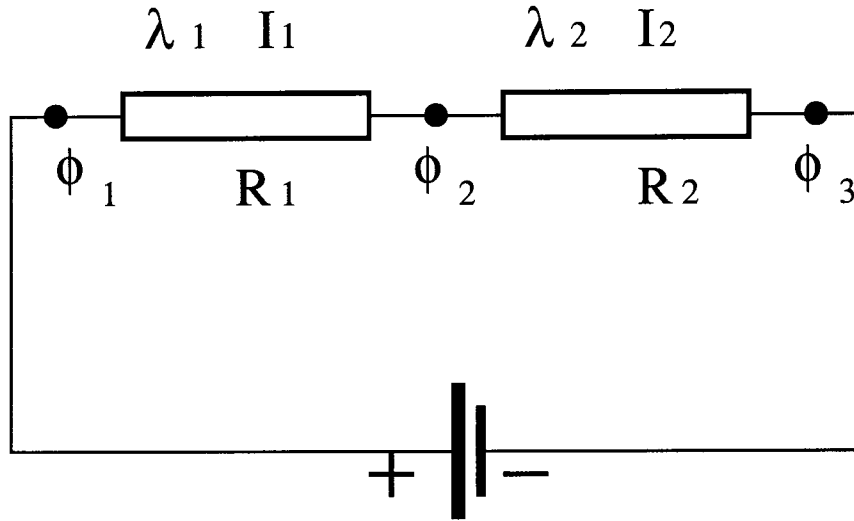


Figure 6.5: An electrical circuit analogy to electroosmotic flow in heterogeneous microchannel in Figure 6.1.

as a function of  $\psi_2$  is relatively small ( $\sim 1$  V) and is due to the assumption of constant surface conductivity  $\lambda_s$  and bulk conductivity  $\lambda_b$  in the simulation. This small variation is induced only by the change in the convective current which is only a small fraction of the conduction current.

As a result, the apparent conductivity for the right section with an EDL effect in Figure 6.1 is higher than that of the left section when bulk conductivity is considered. This difference is attributed to the surface conductance and convection current terms. Furthermore, the small variation of potential  $\phi_2$  with the surface potential  $\psi_2$  is a consequence of the convection current in electroosmotic flow.

### Flow Rate

Figure 6.7 shows the results of the flow rate versus the variation of the surface potential in the section on the right  $\psi_2$  of the heterogeneous channel. In order to eliminate the effect of channel width  $W$  in a 2D simulation problem, the

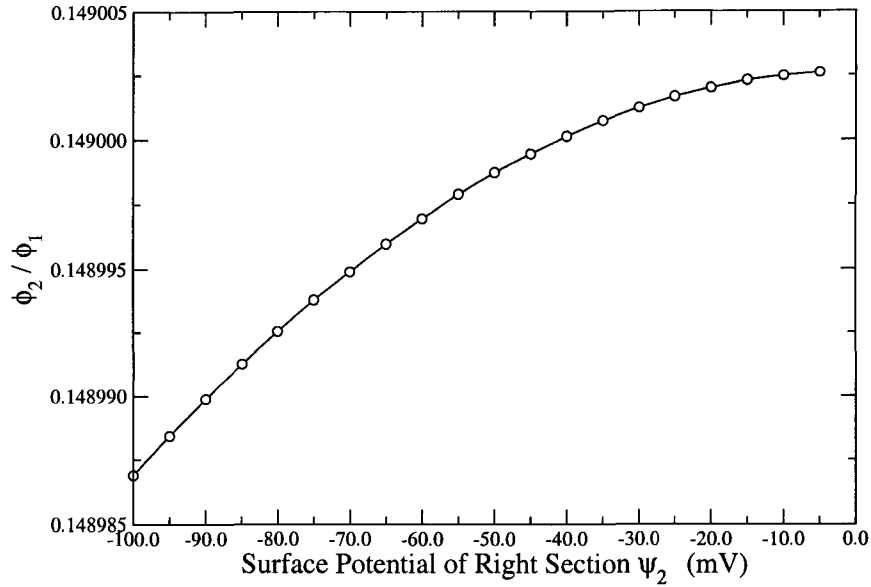


Figure 6.6: Normalized potential at the junction of the two heterogeneous sections in Figure 6.1 versus the surface potential of the right section  $\psi_2$  with current continuity when  $\psi_1 = 0$  mV and  $\phi_1 = 100$  V.

volumetric flow rate is normalized by the maximum flow rate  $Q_{max}$  when the surface potential  $\psi_2$  is  $-100$  mV without consideration of current continuity. In this figure, circles and squares represent the volumetric flow rate with and without the constraint of the current continuity, respectively. As can be seen, the flow rates in both cases are inversely proportional to the negative surface potential, as is well known. However, the flow rate with the constraint of the current continuity is much smaller than that without the constraint. As discussed above, electroosmotic flow is induced by acting the externally applied electric potential on the excess counter-ions in the EDL. In other words, both the externally applied electric potential and EDL will influence the velocity profile and hence volumetric flow rate. For the electroosmotic system simulated in this chapter, the effective driving potential is the difference between  $\phi_2$  and  $\phi_3$  because the surface potential  $\psi_1$  of the left section in Figure 6.1 is zero. Thus,

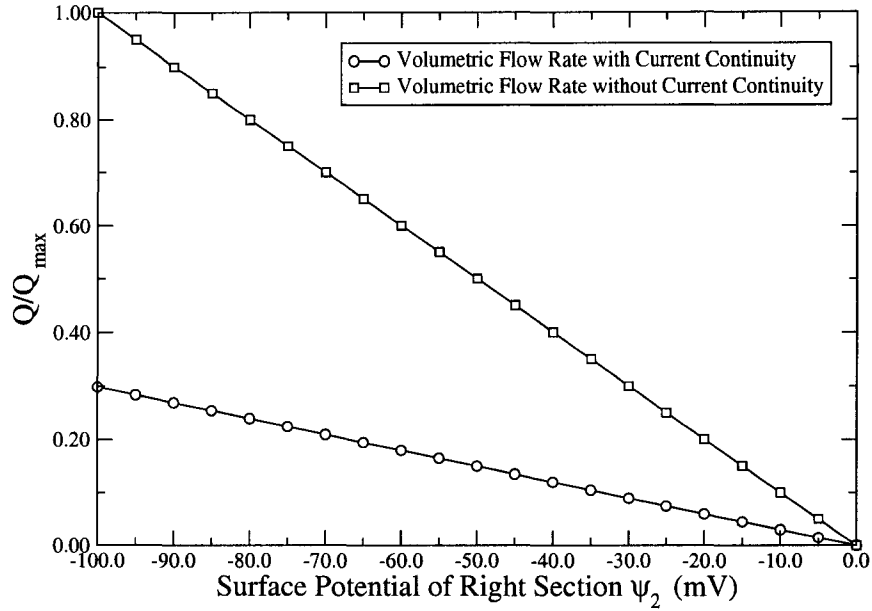


Figure 6.7: Normalized volumetric flow rate in electroosmotic flow versus the surface potential of the right section  $\psi_2$  with and without the constraint of current continuity

the decrease of the potential  $\phi_2$  due to the constraint of current continuity will induce a smaller driving force so that the flow rate will become smaller for the same surface potential. As a result, the flow rate can be overestimated by as much as 70% if the constraint of current continuity is not satisfied in the simulated system.

#### 6.4 Summary

The LBM is used to simulate electrokinetic flow field in a 500 nm channel by consideration of both flow rate and current continuities. For pressure-driven flow, the constraint of current continuity results in the well-known streaming potential effect from the electrical double layer. However, for electroosmotic flow with this constraint under a step variation in surface potential, the potential dis-



tribution along the channel is also a step function. As the potential distribution varies, the effective potential to drive the flow due to an EDL effect decreases significantly and hence the flow rate becomes smaller. The volumetric flow rate without consideration of current continuity could have been overestimated by as much as 70%.

## CHAPTER 7

### CONCLUSIONS AND FUTURE WORK

#### 7.1 Summary of the Results

In this thesis, an equilibrium distribution function in the presence of external forces was employed to derive the lattice Boltzmann equation with an additional (external) force term for microfluidics of electrolyte solution. Coupling with the Poisson-Boltzmann equation for charge distribution, the LBM was used to simulate electroosmotic flow and pressure-driven flow in straight rectangular nano and microchannels. The conclusions are summarized below:

Electroosmotic flow in a straight rectangular microchannel was simulated using a D2Q9 lattice Boltzmann model. Effects of channel height, surface potential, and applied electric field on the velocity profile were studied and compared with the corresponding analytical solutions. Excellent agreement was found. The LBM model considered here is shown to be an effective computational tool for complex microfluidic systems where an externally applied electric field is imposed.

The LBM was used to simulate the electroosmotic flow in nano and microchannels with heterogeneous surface potential. The simulation results indicate that local circulations can occur near a heterogeneous region with nonuni-

form surface potentials, in agreement with those from other studies. Largest circulations, which imply a highest mixing efficiency due to convection and short-range diffusion, were found when the average surface potential is zero, regardless of whether the distribution of the heterogeneous patches is symmetric or asymmetric. A zero average surface potential, however, implies zero flow rate. Therefore, more importantly, it has been illustrated that there is a trade-off between mixing and flow efficiencies in EOF microfluidics. One should not simply focus on mixing and neglect liquid transport. Excellent mixing could lead to a poor transport of electroosmotic flow in microchannels. The results from the simulation can be used as guidelines for the optimization and design of microdevices in terms of mixing and species transport.

The LBM is utilized to simulate electrokinetic flow field in a 500 nm channel by consideration of both flow rate and current continuities. For pressure-driven flow, the constraint of current continuity results in the well-known streaming potential effect from the electrical double layer. However, for electroosmotic flow with this constraint under a step variation in surface potential, the potential distribution along the channel is also a step function. As the potential distribution varies, the effective potential to drive the flow due to an EDL effect decreases significantly so that the flow rate will become smaller for the same surface potential. Therefore, the volumetric flow rate could have been overestimated by as much as 70% without consideration of the current continuity constraint.

## **7.2 Future Work**

The LBM has been demonstrated to be an effective computational tool to simulate the electrokinetic transport phenomena. However, there are still many

interesting questions for further investigation.

1. As mentioned in Chapter 5, the size of the circulation are used to represent the mixing efficiency qualitatively. However, it is necessary to quantify mixing and hence a multicomponent LBM scheme is required. In addition, in the simulation of mixing, charged particles can be involved so that another electrokinetic phenomenon, electrophoresis, can be considered in the LBM model.
2. In this thesis, the ion and potential distribution are governed by the Poisson-Boltzmann equation. The results are only valid for the fully developed region where the charge density was assumed to follow the Boltzmann equilibrium distribution. The effect of entry and multidirection flow field on the ion distribution has been neglected. To investigate the effect of entry region and the multidirection flow on the flow characteristics without assuming the Boltzmann equation for ion density distribution, the Nernst-Planck equation, also called convection-diffusion-migration (CDM) equation, should be coupled with the LBM method. This CDM equation can be solved by LBM method. In the future work, an appropriate LBM scheme should be developed to solve for the ion and potential distribution and flow field simultaneously.
3. The geometry of the channel in the simulation is simple so that the boundary condition can be easily implemented. For a more complex geometry in other applications, a complicated boundary condition is required for more accurate results.

## BIBLIOGRAPHY

- [1] J. H. Ferziger and M. Peric. *Computational Methods for Fluid Dynamics*. Springer, 2002.
- [2] P. Roach. *Computational Fluid Dynamics*. Hermosa Publishing, 1972.
- [3] J. Connor and C. Brebbia. *Finite Element Techniques for Fluid Flow*. Newnes-Butterworths, 1976.
- [4] J. Dupuy and A. Dianoux. *Microscopic Structure and Dynamics of Liquids*. Plenum Press, 1978.
- [5] J. Goodfellow. *Molecular Dynamics*. Macmillan Press, 1991.
- [6] G. Bird. Recent advances and current challenges for DSMC. *Computers Math. Applic.*, 35:1, 1998.
- [7] E. S. Oran, C. K. Oh, and B. Z. Cybyk. Direct simulation monte carlo: Recent advances and applications. *Ann. Rev. Fluid Mech.*, 30:403, 1998.
- [8] D. A. Wolf-Gladrow. *Lattice-Gas Cellular Automata and Lattice Boltzmann Models*. Springer, 1991.
- [9] U. Frisch, B. Hasslacher, and Y. Pomeau. Lattice-gas automata for the Navier-Stokes equation. *Phys. Rev. Lett.*, 56:1505, 1986.

- [10] P. L. Bhatnagar, E. P. Gross, and M. Krook. A model for collision processes in gases I: Small amplitude processes in charged and neutral one-component systems. *Phys. Rev. Lett.*, 94:511, 1954.
- [11] F. F. Ruess. *Memoires de la Societe Imperiale de naturalistes de Moscou*, 2:327, 1809., 2:327, 1809.
- [12] G. Quinke. *Pogg. Ann. Physik*, 1:107, 1859.
- [13] R. J. Hunter. *Introduction to Modern Colloid Science*. Oxford Science Publication, 1993.
- [14] R. J. Hunter. *Foundations of Colloid Science*. Oxford University Press, New York, 2nd ed., 2001.
- [15] J. Lyklema. *Fundamentals of Interface and Colloid Science, volume II*. Academic Press, 1995.
- [16] D. Burgreen and F. R. Nakache. Electrokinetic flow in ultrafine capillary slits. *J. Phys. Chem.*, 68:1084, 1963.
- [17] C. L. Rice and R. Whitehead. Electrokinetic flow in a narrow cylindrical capillary. *J. Phys. Chem.*, 69:4017, 1965.
- [18] S. Chen and G. D. Doolen. Lattice Boltzmann method for fluid flow. *Annu. Rev. Fluid Mech.*, 30:329, 1998.
- [19] X. He and L. S. Luo. Theory of the lattice boltzmann method: From the Boltzmann equation to the lattice Boltzmann equation. *Phys. Rev. E*, 1997.
- [20] L. S. Luo. Theory of the lattice Boltzmann method: Lattice Boltzmann models for non-ideal gases. *Phys. Rev. E*, 62:4982, 2002.

- [21] H. Yu, L. S. Luo, and S. S. Girimaji. Scalar mixing and chemical reaction simulations using lattice Boltzmann method. *Intern. J. Comput. Engeer. Sci.*, 3(1):73, 2002.
- [22] S. Succi, R. Benzi, and F. Higuera. The lattice Boltzmann - a new tool for computational fluid dynamics. *Physica D*, 47:219, 1991.
- [23] S. Chen, Z. Wang, X. W. Shan, and G. D. Doolen. Lattice Boltzmann computational fluid dynamics in three dimensions. *J. Stat. Phys*, 68:379, 1992.
- [24] D. R. Noble, J. G. Georgiadis, and R. O. Buchius. Comparison of accuracy and performance for lattice Boltzmann and finite difference simulation of steady viscous flow. *Int. J. Numer. Meth. Fluids*, 23:1, 1996.
- [25] S. Succi. *The Lattice Boltzmann Equation for Fluid Dynamics and Beyond*. Clarendon press, Oxford, 2001.
- [26] N. S. Martys and H. Chen. Simulation of multicomponent fluids in complex three-dimensional geometries by the lattice boltzmann method. *Phys. Rev. E*, 53:743, 1996.
- [27] X. Shan. Simulation of nonideal gases and liquid-gas phase transitions by the lattice Boltzmann equation. *Phys. Rev. E*, 49:2941, 1994.
- [28] X. Shan and H. Chen. Lattice boltzmann model for simulating flows with multiple phases and components. *Phys. Rev. E*, 47:1815, 1993.
- [29] J. Zhang, B. Li, and D. Y. Kwok. A mean-field free-energy approach to lattice Boltzmann method for liquid-vapor and solid-fluid interfaces. *Phys. Rev. E*, 69:032602-1, 2004.

- [30] B. Li and D. Y. Kwok. Lattice Boltzmann model of microfluidics with high reynolds number in the presence of external forces. *Langmuir*, 19:3041, 2003.
- [31] M. Gardener. The fantastic combination of John Conway's new solitaire game life. *Scientific American*, 220:120, 1970.
- [32] J. Hardy, Y. Pomeau, and O. Pazzis. Time evolution of two-dimensional model system I: Invariant state and time correlation functions. *J. Math. Phys.*, 14:1746, 1973.
- [33] J. Hardy, O. Pazzis, and Y. Pomeau. Molecular dynamics of classical lattice gas: Transport properties and time correlation functions. *Phys. Rev. A*, 13:1949, 1976.
- [34] U. Frisch, B. Hasslacher, and Y. Pomeau. Lattice-gas automata for the Navier-Stokes equation. *Phys. Rev. Lett.*, 56:1505, 1986.
- [35] S. Wolfram. Cellular automaton fluids 1: Basic theory. *J. Stat. Phys.*, 45:526, 1986.
- [36] U. Frisch, D. d'Humières, B. Hasslacher, P. Lallemand, Y. Pomeau, and J. P. Rivet. Lattice gas hydrodynamics in two and three dimensions. *Complex Systems*, 1:649, 1987.
- [37] B. Chopard and M. Droz. *Cellular Automata Modelling of Physical Systems*. Cambridge University Press, 1998.
- [38] D. d'Humières, P. Lallemand, and U. Frish. Lattice gas model for 3D hydrodynamics. *Europhys. Lett.*, 2:291, 1986.



- [39] G. McNamara and G. Zanetti. Use of the Boltzmann equation to simulate lattice gas automata. *Phys. Rev. Lett.*, 61:2332, 1988.
- [40] F. Higuera and J. Jimenez. Boltzmann approach to lattice gas simulations. *Europhys. Lett.*, 9:663, 1989.
- [41] J. M. V. A. Koelman. A simple lattice Boltzmann scheme for Navier-Stokes fluid flow. *Europhys. Lett.*, 15:603, 1991.
- [42] Y. H. Qian, D. d’Humières, and P. Lallemand. Lattice BGK models for Navier-Stokes equation. *Europhys. Lett.*, 17:479, 1992.
- [43] C. Cercignani. *Mathematical Methods in Kinetic Theory*. Plenum, 1990.
- [44] F. Higuera, J. Jimenez, and S. Succi. Lattice gas dynamics with enhanced collision. *Europhys. Lett.*, 9:345, 1989.
- [45] S. Chen, H. Chen, D. Martinez, and W. Matthaeus. Lattice Boltzmann model for simulation of magnetohydrodynamics. *Phys. Rev. Lett.*, 1991.
- [46] Y. H. Qian, S. Succi, and S. A. Orszag. Recent advances in lattice Boltzmann computing. *Annual Reviews of Computational Physics III*, page 195, 1995.
- [47] B. Li and D. Y. Kwok. Discrete Boltzmann equation for microfluidics. *Phys. Rev. Lett.*, 90(12), 03 2003.
- [48] N. S. Martys, X. Shan, and H. Chen. Evaluation of the external force term in the discrete Boltzmann equation. *Phys. Rev. E*, 58:6855, 1998.
- [49] S. Chapman and T. G. Cowling. *The Mathematical Theory of Non-Uniform Gases*. Cambridge University Press, 1970.

- [50] D. R. Noble, S. Chen, J. G. Georgiadis, and R. O. Bukius. A consistent hydrodynamic boundary condition for the lattice Boltzmann method. *Phys. Fluids*, 7:203, 1995.
- [51] D. R. Noble, J. G. Georgiadis, and R. O. Bukius. Direct assessment of lattice Boltzmann hydrodynamics and boundary conditions for recirculating flows. *J. Stat. Phys*, 81:17, 1995.
- [52] T. Inamuro, M. Yoshino, and F. Ogino. A non-slip boundary condition for lattice Boltzmann simulations. *Phys. Fluids*, 7:2928, 1995.
- [53] P. A. Skordos. Initial and boundary conditions for the lattice Boltzmann method. *Phys. Rev. E*, 48:4823, 1993.
- [54] R. Cornubert, D. d'Humières, and D. Levermore. A Knudsen layer theory for lattice gases. *Physica D*, 47 (6):241, 1991.
- [55] H. L. F. Helmholtz. *Wied. Ann.*, 7:337, 1879.
- [56] G. Gouy. *J. Phys. Radium*, 9:457, 1910.
- [57] D. L. Chapman. *Phil. Mag.*, 25:475, 1913.
- [58] J. H. Masliyah. *Electrokinetic Transport Phenomena*. OSTRATECH technical publication series ; no. 12. Edmonton, Alta. : Alberta Oil Sands Technology and Research Authority, 1994.
- [59] Z. H. Fan and D. J. Harrison. Micromachining of capillary electrophoresis injectors and separators on glass chips and evaluation of flow at capillary intersections. *Anal. Chem.*, 66:177, 1994.

- [60] D. R. Briggs. The determinations of the  $\zeta$  - potential on cellulose – A method. *J. Phys. Chem.*, 32:641, 1928.
- [61] A. Rutgers. *Trans. Faraday Soc.*, 36:69, 1940.
- [62] N. A. Patankar and H. H. Hu. Numerical simulation of electroosmotic flow. *Anal. Chem.*, 70:1870, 1998.
- [63] F. Bianchi, R. Ferrigno, and H. H. Girault. Finite element simulation of an electroosmotic-driven flow division at a T-junction of microscale dimension. *Anal. Chem.*, 72:19887, 2002.
- [64] A. D. Stroock, M. Weck, D. T. Chiu, W. T. S. Huck, P. J. A. Kenis, R. F. Ismagilov, and G. M. Whitesides. Patterning electro-osmotic flow with patterned surface charge. *Phys. Rev. Lett.*, 84:3314, 2000.
- [65] D. R. Meldrum and M. R. Holl. Microscale bioanalytical systems. *Science*, 297:1197, 2002.
- [66] T. Thorsen, S. J. Maerkl, and S. R. Quake. Microfluidic large-scale integration. *Science*, 298:580, 2002.
- [67] T. Stadter. How microfluidics works. *Tech. Rev.*, 105:77, 2002.
- [68] S. Arulandam and D. Li. Liquid transport in rectangular microchannels by electroosmotic pumping. *Colloids and Surfaces A*, 161:89, 2000.
- [69] A. T. Conlisk and J. McFerran. Mass transfer and flow in electrically charged micro- and nanochannels. *Anal. Chem.*, 74:2139, 2002.
- [70] P. Dutta, T. C. Warburton, and A. Beskok. Numerical modeling of electroosmotically driven microflows. *J. MEMS*, 1:467, 1999.

- [71] G. Bird. Monte Carlo simulation of gas flow. *Ann. Rev. Fluid Mech.*, 10:11, 1978.
- [72] M. P. Allen and D. J. Tildesley. *Computer Simulation of Liquid*. Oxford Science Publication, 1994.
- [73] R. Qiao and N. R. Aluru. Transient analysis of electroosmotic flow in nanodiameter channels. *Computational Nanoscience and Nanotechnology*, ISBN 0-9708275-6-3, 2002.
- [74] R. Qiao and N. R. Aluru. Ion concentrations and velocity profiles in nanochannel electroosmotic flows. *J. Chem. Phys.*, 118:4692, 2003.
- [75] U. Frisch, B. Hasslacher, and Y. Pomeau. Lattice-Gas Automata for the Navier-Stokes equation. *Phys. Rev. Lett.*, 56:1505, 1986.
- [76] B. Li, S. Chai, F. Tian, and D. Y. Kwok. A flexible lattice Boltzmann model of microfluidics in the presence of external forces. In A. A. Mohamad, editor, *Proceedings of the 3ICCHMT*, page 414, 2003.
- [77] F. Tian, B. Li, and D. Y. Kwok. Simulation of electroosmotic flows in nano and microchannels using lattice Boltzmann model. *J. Comput. Theor. Nanosci.*, 2003. Accepted.
- [78] F. Tian, B. Li, and D. Y. Kwok. Lattice Boltzmann simulation of microfluidics with non-uniform zeta potentials: Requirements of flow rate and current continuities. In *Proceeding of the 2004 International conference on MEMS, NANO, and smart systems*, 2004. Accepted.
- [79] R. H. Liu, M. A. Stremmer, K. V. Sharp, M. G. Olsen, J. G. Santiago, R. J. Adrian, H. Aref, and D. J. Beebe. Passive mixing in a three-dimensional ser-

- pentine microchannel. *Journal of Microelectromechanical System*, 9(2):190, 2000.
- [80] A. D. Stroock, S. K. W. Dertinger, A. Ajdari, I. Mezic, H. A. Stone, and G. M. Whitesides. Chaotic mixer for microchannels. *Science*, 295:647, 2002.
- [81] A. D. Stroock, S. K. Dertinger, G. M. Whitesides, and A. Ajdari. Patterning flows using grooved surfaces. *Anal. Chem.*, 74:5306, 2002.
- [82] Y. K. Lee, J. Deval, P. Tabeling, and C. M. Ho. Chaotic mixing in electrokinetically and pressure driven micro flows. *Proc. 14 th IEEE Workshop on Micro Electro Mechanical Systems (Interlaken, Switzerland, Jan.)*, page 483, 2001.
- [83] M. H. Oddy, J. G. Santiago, and J. C. Mikkelsen. Electrokinetic instability micromixing. *Anal. Chem.*, 73:5822, 2001.
- [84] R. J. Yang, L. M. Fu, and Y. C. Lin. Electroosmotic flow in microchannels. *J. Colloid and Interface Sci.*, 239:98, 2001.
- [85] A. Ajdari. Electro-osmosis on inhomogeneously charged surface. *Phys. Rev. Lett.*, 75:755, 1995.
- [86] A. Ajdari. Generation of transverse fluid currents and forces by an electric field: Electro-osmosis on charge-modulated and undulated surfaces. *Phys. Rev. E*, 53:4996, 1996.
- [87] R. B. M. Schasfoort, S. Schlautmann, J. Hendrikse, and A. van den Berg. Field-effect flow control for microfabricated fluidic networks. *Science*, 286:942, 1999.

- [88] J. Yang and D. Y. Kwok. Microfluid flow in circular microchannel with electrokinetic effect and navier's slip condition. *Langmuir*, 19:1047, 2003.
- [89] J. Yang and D. Y. Kwok. Analytical treatment of flow in infinitely extended circular microchannels and the effect of slippage to increase flow efficiency. *J. Micromech. Microeng.*, 13:115, 2003.
- [90] J. Yang and D. Y. Kwok. Effect of liquid slip in electrokinetic parallel-plate micro channel flow. *J. Colloid Interface Sci.*, 260:265, 2003.
- [91] J. Yang, A. Bhattacharyya, J. H. Masliyah, and D. Y. Kwok. Oscillating laminar electrokinetic flow in infinitely extended rectangular microchannels. *J. Colloid Interface Sci.*, 261:21, 2003.
- [92] J. Yang and D. Y. Kwok. Time-dependent laminar electrokinetic slip flow in infinitely extended rectangular microchannels. *J. Chem. Phys.*, 118:354, 2003.
- [93] J. Yang, J. H. Masliyah, and D. Y. Kwok. Streaming potential and electroosmotic flow in heterogeneous circular microchannels with non-uniform zeta potentials: Requirements of flow rate and current continuities. *Langmuir*, Mar 2004. accepted.
- [94] D. Erickson, D. Li, and C. Werner. An improved method of determining the  $\zeta$ -potential and surface conductance. *J. Colloid Interface Sci.*, 232:186, 2000.